8. Fractal Geometry

Clouds are not spheres, mountains are not cones, coastlines are not circles, and bark is not smooth, nor lightenings travel in a straight line.

Benoit Mandelbrot

What really interests me is whether God had any choice in the creation of the world.

Albert Einstein

Fractals in nature originate from self-organized critical dynamical processes.

Per Bak and Kan Chen (1989)

Since Euclid (300 BC) we have been used to perceiving nature with the concept of a three-dimensional (3-D) geometry. We measure linear structures in one dimension, area-like structures in two dimensions, and volume-like structures in three dimensions. However, when we measure an object in terms of these three dimensions, we are aware that the geometric model describes a solid body, while a natural object may be inhomogeneous, porous, or even mostly empty, if we think on atomic scales. The counterpart to Euclidean geometry, the set theory with discrete elements, has been introduced by mathematicians like Georg Cantor, Karl Weierstrass, and Augustin-Louis Cauchy. The mathematical concept of discrete, irregular, inhomogeneous structures has then been discovered in the real world by Benoit Mandelbrot, who coined the definition of a *fractal dimension*, which represents a generalization (in terms of rational or irrational numbers) to the *Euclidean dimension* (which is restricted to integer values of 1, 2, 3, or *n*). A fractal dimension is a scale-free quantity that describes the fractional filling of a structure over some scale range, but usually does not extend to infinite microscopic or macroscopic scales. Popular examples are the coastline of Norway, ferns, trees, mountain landscapes, snowflakes, or clouds. The reason why we dedicate a chapter to fractal geometry here is, of course, because self-organized criticality also is governed by scale-free powerlaw distributions of observable parameters. Therefore, fractal geometry is nothing else than the spatial counterpart of self-organized criticality processes observed in the temporal and energy domain. In a paper

entitled "The physics of fractals", Bak and Chen (1989) succinctly summarized *Fractals in nature originate from self-organized critical dynamical processes.*

General introductions to fractal geometry can be found in textbooks like *Fractals* (Mandelbrot 1977), *The Fractal Geometry of Nature* (Mandelbrot 1983), *The Beauty of Fractals* (Peitgen and Richter 1986), *Fractals Everywhere* (Barnsley 1988), *The Science of Fractal Images* (Peitgen and Saupe 1988), *Fractals, Chaos, Power Laws* (Schroeder 1991), *Critical Phenomena in Natural Sciences: Chaos, Fractals, Selforganization and Disorder* (Sornette 2004), *Discovery of Cosmic Fractals* (Baryshev and Teerikorpi 2002), or *Fractals and Chaos in Geology and Geophysics* (Turcotte 1997). Related articles can also be found in *The Physics of Fractals* (Bak and Chen 1989) and in popular articles like *The Language of Fractals* (Juergens et al. 1990) or *Chaos and Fractals in Human Physiology* (Goldberger et al. 1990). In the following we focus mostly on measurements of fractal dimensions or related spatial parameter distributions from astrophysical observations, which we relate to other SOC parameter distributions. Fractal structures were found in magnetospheric phenomena, solar flares, planetary systems, stardust, galactic structures, and cosmology.

8.1 1-D Fractals

In the next three sections we divide the discussion of fractal dimensions by their approximate spatial dimension, but this should not be taken too literally, because it is an intrinsic property of fractal structures that they deviate from a strict Euclidean dimension. One-dimensional structures are lines, segments of lines, contours, which can be straight, curved, intermittent, discrete, folded, intertwined, or deformed by any conceivable transform. If there is a repetitive pattern on different scales, such structures can be self-similar and fractal. Fractal structures are most naturally generated by a replication process that works in a self-similar way at different scales. For instance the growth of crystals occurs in subsequent layers that replicates the original molecular grid structure. Therefore, also the mathematical definition of fractal geometries usually makes use of a simple transformation rule that is repeated on successive size scales.

8.1.1 The Cantor Set and Koch Curve

A Cantor set, also called "Cantor dust", is a subdivision of a set into smaller pieces with a fixed fraction in each subsequent step. With progressive iterations, the number of elements increases to infinity, but their total length approaches zero. For instance, in the Cantor set shown in Fig. 8.1, a bar is subdivided into two bars by erasing the middle third, so the number of elements increases as $N = 2^i$ with every iteration i, while the length decreases as $\varepsilon = (1/3)^i$. In mathematical language, the set is uncountable but has a measure of zero. The Hausdorff dimension D of a one-dimensional fractal structure is defined as a powerlaw relation between the number N of elements and the length scale ε of an element,

$$N(\varepsilon) \propto \varepsilon^{-D} \qquad \text{for } \varepsilon \mapsto 0 , \tag{8.1.1}$$

Fig. 8.1 Construction of the "middle-third-erasing" Cantor set: The replication rule is to eliminate the middle third of every bar in subsequent subdivisions. The total length converges to zero, while the fractal dimension is $D = \log(2)/\log(3) = 0.630930....$

and quantifies how the number N of elements depends on the size scale ε. Thus, we can obtain the Hausdorff dimension D from $N = 2^i$, $\varepsilon = (1/3)^i = 3^{-i}$, and Eq. (8.1.1),

$$D = -\frac{\log N}{\log \varepsilon} = \frac{\log 2}{\log 3} \approx 0.630930.... \ , \tag{8.1.2}$$

for this Cantor set. The fact that the fractal dimension D is smaller than the Euclidean value of $D = 1$ means that the 1-D structure has less than solid filling, and if the fractal process is continued to infinitely microscopic scales, it even approaches a total length of zero. Perhaps our whole universe has this fractal property if we probe matter down to microscopic scales, or even down to atomic and sub-atomic scales.

A classical example of a fractal one-dimensional structure is the Koch curve (Fig. 8.2). The initiator function is a straight line. A generator function is constructed by replacing the middle third by an equilateral triangle, so that the length of the fractal generator function is 4 units, while the size of the initiator function is 3 units. In subsequent iterations, each straight segment is replaced by another generator function (Fig. 8.2). The number of segments thus increases a factor of 4 with each iteration ($N = 4^i$), while the length of each segment becomes a factor 3 smaller each time ($\varepsilon = (1/3)^i = 3^{-i}$), which yields the Hausdorff dimension

$$D = -\frac{\log N}{\log \varepsilon} = \frac{\log 4}{\log 3} \approx 1.26186.... \ , \tag{8.1.3}$$

Note that the fractal dimension is now larger than the Euclidean dimension $D = 1$ of a straight or smooth line, which indicates that the line is increasingly folded in a meandering pattern with smaller scales. Famous examples of this fractal structure is the coastline of Norway or Great Britain, which both became eroded by many fjords, valleys, rivers, streams, and creeks, so that the ragged coastal length increases the finer the spatial resolution of the topographical map is.

8.1.2 Irregularity of Time Series

Every type of one-dimensional data can be investigated in terms of fractal analysis. For instance, a string of binary data (e.g., 0 0 1 0 1 1 1 0 1 0 1 1 1 0 1 0 0 1 0 1 1 0) or a Morse code (e.g., ...—...-.-....—-.-.–..) resemble pretty much the Cantor set shown in
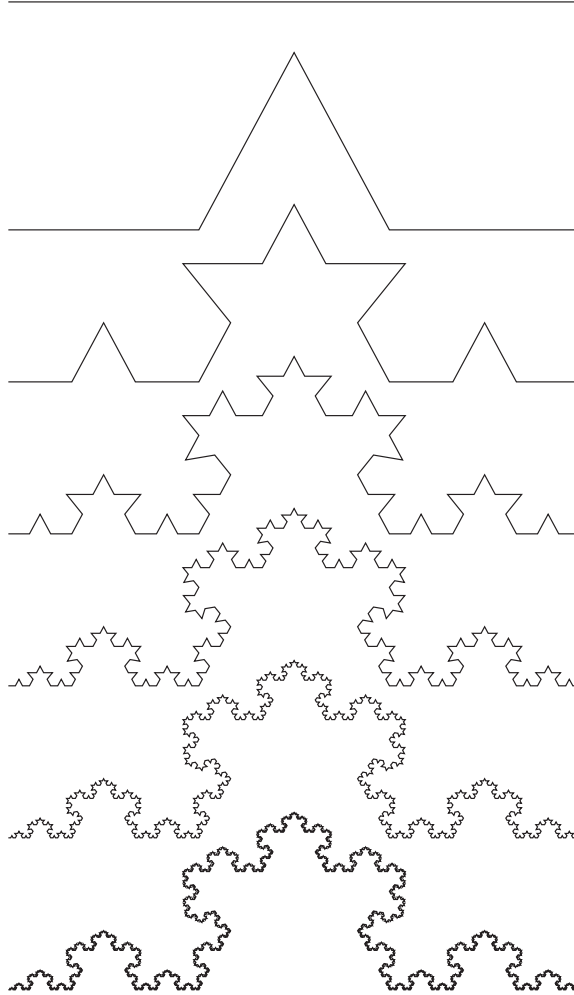
Fig. 8.2 Construction of the "Koch curve": The generator function consists of three segments, with an equilateral triangle in the middle third, forming four straight segments of equal length. Six successive iterations are shown, where each straight segment is replaced by the fractal generator function.

Fig. 8.1, and thus a Hausdorff dimension (Eq. 8.1.1) can be determined, regardless whether the pattern is regular or irregular. However, a structure is only fractal, when the value of the Hausdorff dimension is found to be invariant at different scales, which means that the ratio of $\log(N)$ to $\log(\varepsilon)$ is constant, and thus implies a powerlaw behavior.

While the Cantor set (Fig. 8.1) represents a binary structure, 1-D data are generally multi-valued, such as a time series $f_i = f(t_i)$ with values in a range of $f_{min} \leq f_i \leq f_{max}$. A technique to measure the fractal dimension of a set of points $[t_i, f_i = f(t_i)]$ forming a graph or time profile of a function f has been developed by Higuchi (1988). The technique is normalized in such a way that a fractal dimension of $D = 1$ corresponds to a

completely regular time profile (such as a constant or slowly-varying smooth time profile), but approaches the value of $D = 2$ for a completely irregular time series. Thus, the fractal dimension is a measure of the irregularity or complexity of a time profile. Let us consider a time series of values $f_i = f(i)$ as a function of the time step $i = 1, ..., N$,

$$f(1), f(2), f(3), ..., f(N) . \tag{8.1.4}$$

Then we generate subsets of time series with different time steps $k = 1, 2, 3, ...$, starting at all possible phases $m = 1, 2, 3, ..., k$,

$$f(m), f(m+k), f(m+2k), f(m+3k), ..., f(m+[(N-m)/k]k) . \tag{8.1.5}$$

For each time step k and phase m we can now define a length $L_m(k)$,

$$L_m(k) = \frac{1}{k} \left[\left(\sum_{i=1}^{|(N-m)/k|} |f(m+ik) - f(m+(i-1)k)| \right) \frac{N-1}{[(N-m)/k]k} \right] \tag{8.1.5}$$

Since we are interested in a time scale spectrum, but not in the phases m, we average the length $L_m(k)$ over all phases m and obtain a mean value $\langle L_m(k) \rangle$ for every time step k. If the length $\langle L_m(k) \rangle$ shows a powerlaw dependence on the time step k, the time series has a fractal dimension D,

$$\langle L_m(k) \rangle \propto k^{-D} . \tag{8.1.6}$$

Higuchi (1988) applied this algorithm to a time series of a fractional Brownian function, which has the property of self-similarity on all scales, and determined with this method the precise value of its fractal dimension $D = 2$.

8.1.3 Variability of Solar Radio Emission

The fractal analysis of Higuchi (1988) has been applied to time series of solar radio emission by Watari (1996a). The analyzed data consist of nine time series of daily solar radio fluxes at different frequencies from $\nu = 245$ MHz to $\nu = 15.4$ GHz, observed during the years 1976–1990, published in the *Solar-Geophysical Data* catalog, as well as the time series of the sunspot number. Thus the time resolution of the data is 1 day and the length is 15 years (i.e., 5,479 days or datapoints for each set). The time series are shown in Fig. 8.3, which all represent measures of the solar cycle variability observed at different wavelengths, different physical conditions, and different physical emission mechanisms. The measurement of the fractal dimension (Eq. 8.1.6) requires a time scale spectrum $\langle L_m(k) \rangle$, which are shown in Fig. (8.4), calculated in a range from $k = 1$ day to $k = 40$ days. Since a half solar rotation represents the longest possible time interval during which a solar radio source can be observed contiguously, the time series is expected to change its behavior at $k \lesssim 13$ days. The time scale spectra $\langle L_m(k) \rangle$ shown in Fig. 8.4 clearly show a powerlaw behavior at all frequencies in the range of $k \approx 1$–10 days, while a drop-off is visible in the range of $k \approx 10$–40 days, as expected from the solar rotation effect.
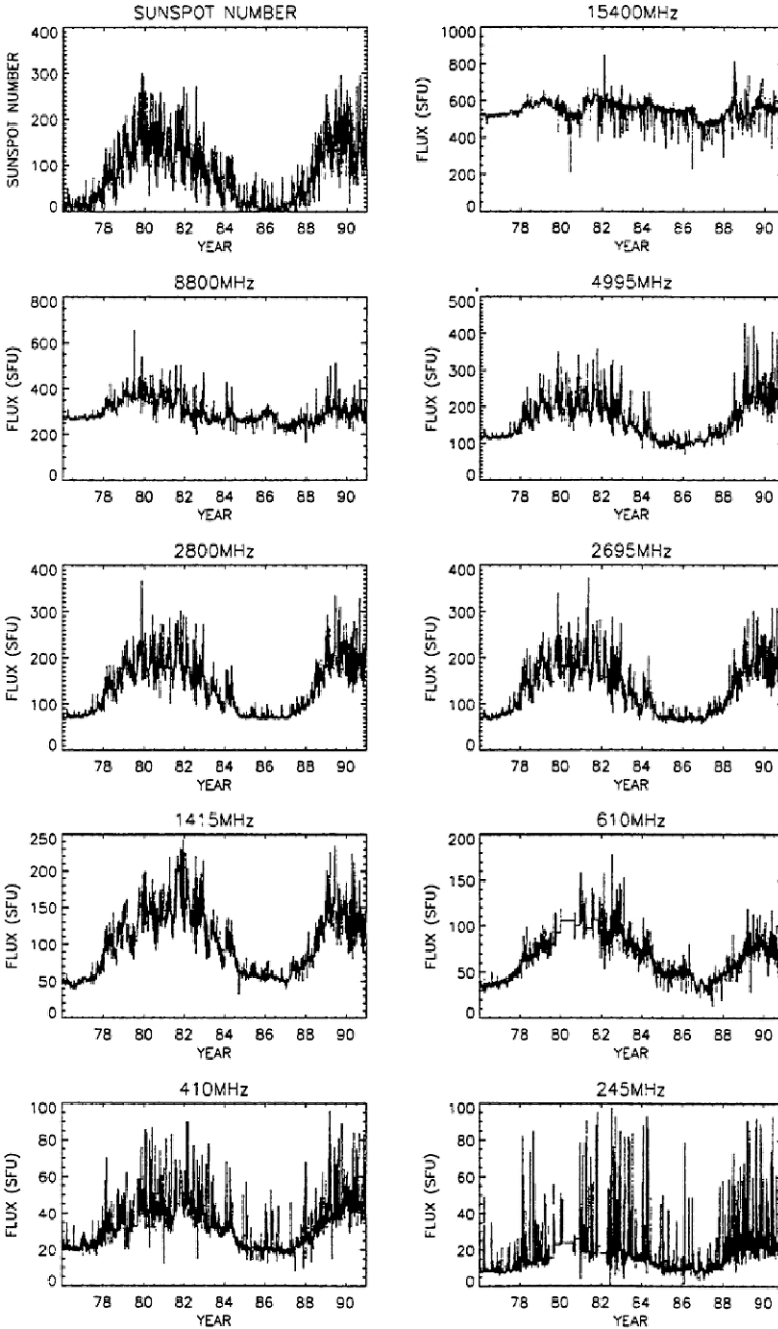
Fig. 8.3 Time profiles of the daily sunspot number (top left) and daily solar radio fluxes at frequencies of 245, 410, 610, 1,415, 2,695, 2,800, 4,995, 8,800, and 15,400 MHz (Watari 1996a).
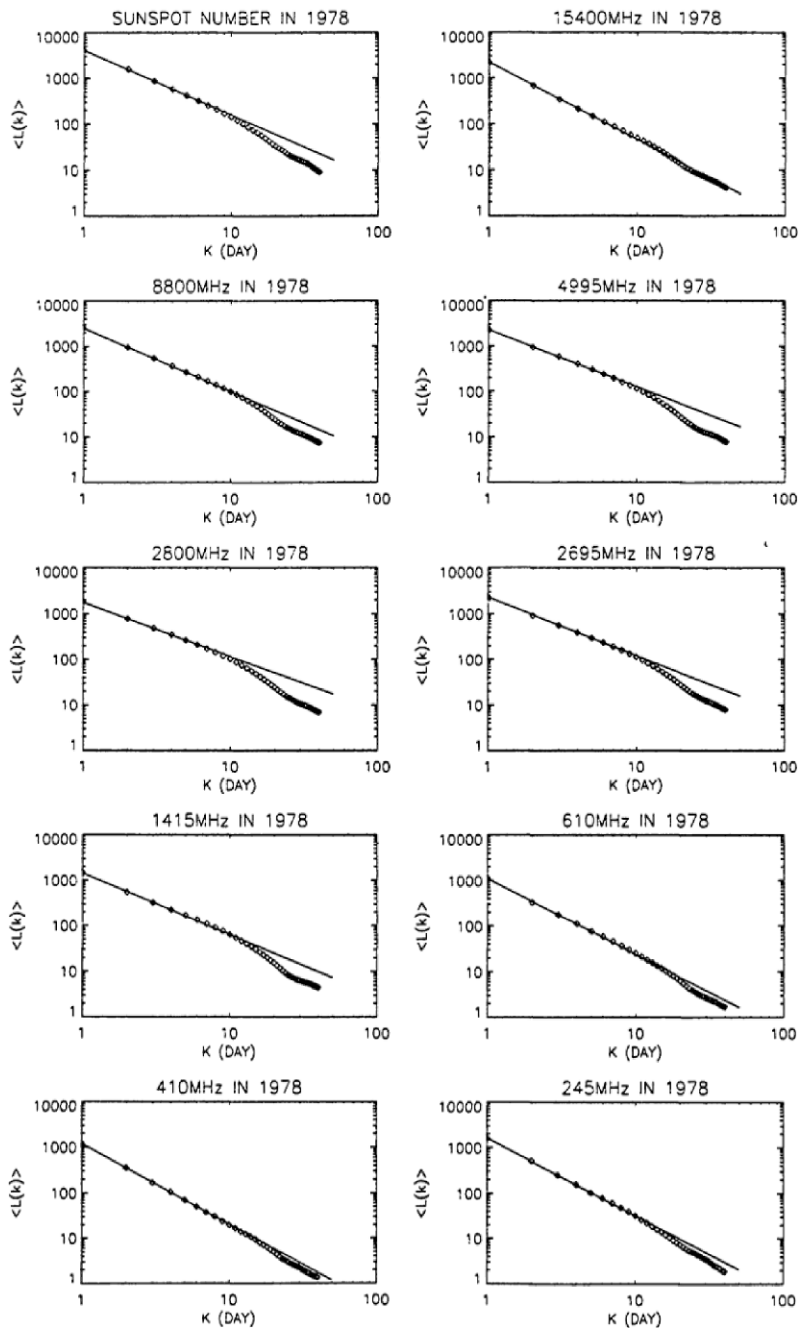
Fig. 8.4 Time scale spectrum $\langle L_m(k)\rangle$ of the 10 time series shown in Fig. 8.3 (Watari 1996a).
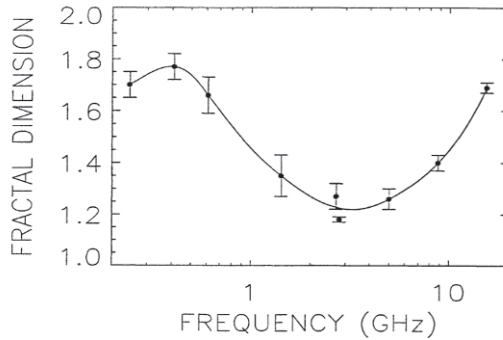
Fig. 8.5 Variation of the fractal dimension $D(\nu)$ as a function of the radio frequency ν from the year 1978, at the beginning of the solar cycle 21 (Watari 1996a).

An interesting result that came out of this study, besides the fractality of solar radio emission, is the dependence of the fractal dimension $D(\nu)$ on the radio frequency ν, which is shown in Fig. 8.5. There is a variation from a lowest fractal dimension of $D \approx 1.2$ at frequencies of $\nu \approx 2\text{--}5$ GHz, to the highest fractal dimension with values of $D \approx 1.8$ at frequencies of 400 MHz, as well as near 15 GHz. This difference in the fractal dimension is likely to be a consequence of different radiation mechanisms. At decimetric frequencies ($\nu \approx 0.3 - 3.0$ GHz), solar radio emission is dominated by so-called *decimetric type III bursts*, which are caused by a beam-driven bump-in-tail instability producing plamsa emission. Such type III-like bursts occur very sporadically and irregularly due to the nonlinear nature of plasma instabilities, and thus can explain the high value of the fractal dimension measured in the $\nu \approx 0.3\text{--}1.0$ GHz range. At higher frequencies, gyroresonance emission in strong magnetic fields, such as above sunspots, is the most dominant radio emission (e.g., Dulk 1985). Since the strong magnetic field above sunspots has a slowly-varying time evolution, this could explain the lower fractal dimension of $D \approx 1.2\text{--}1.3$ at radio frequencies of $\nu \approx 1\text{--}5$ GHz. This is also corroborated by the fact that Watari (1996a) found a similar low fractal dimension of $D \approx 1.2$ for the variability of the sunspot number. The third frequency domain at $\nu \gtrsim 10$ GHz, is too high to contain significant gyroresonance emission, and thus could be dominated by free-free bremsstrahlung from flare events, which occur very sporadically (see monthly averages in hard X-rays in Fig. 7.6), which could explain the upturn to a higher fractal dimension (Fig. 8.5) observed by Watari (1996a). In conclusion, the fractal dimension of the time series seems to provide a sensible diagnostic of physical emission mechanisms with different time variability characteristics.

8.2 2-D Fractals

By 2-D fractals we mean structures that can be measured from 2-D data, such as a flat or slightly curved image, as they are produced in abundance from CCD readouts of astronomical telescopes. If an image is strictly flat, any extracted structure can have a fractal dimension in the range of $D = 0, ..., 2$. Essentially, solid blobs appearing in an image have

an Euclidean dimension of $D = 2$, curvilinear structures a dimension near $D = 1$, and dots a dimension near $D = 0$. A nice selection of fractal structures sorted by their dimension can be viewed on the wikipedia website (http://en.wikipedia.org/wiki/List_of_fractals_by_Hausdorff_dimension).

8.2.1 Hausdorff Dimension and Box-Counting Method

For Euclidean structures, the area A of a square is a quadratic function of the length scale or size L, i.e., $A = L^D$ with Euclidean dimension $D = 2$. If we cover the area A of linear size L with n squares, we have $n = L^D$ and can define an Euclidean dimension D by

$$D = \frac{\log n(L)}{\log L} \ , \tag{8.2.1}$$

which is also valid for other Euclidean dimensions $D = 1$ or $D = 3$. The same definition is extended to fractal structures, called the *Hausdorff dimension*, where D generally is a non-integer number,

$$D = \lim_{\varepsilon \to 0} \frac{\log n(\varepsilon)}{\log(1/\varepsilon)} \ , \tag{8.2.2}$$

where $n(\varepsilon)$ is the number of self-similar structures of linear size $\varepsilon = 1/L$ that are needed to cover the whole structure. In Fig. 8.6 we show the iterative generation of the Sierpinski triangle, which is constructed by subdividing an equilateral triangle into four smaller triangles of half the size in each iteration step. Thus the fractal dimension of the Sierpinski
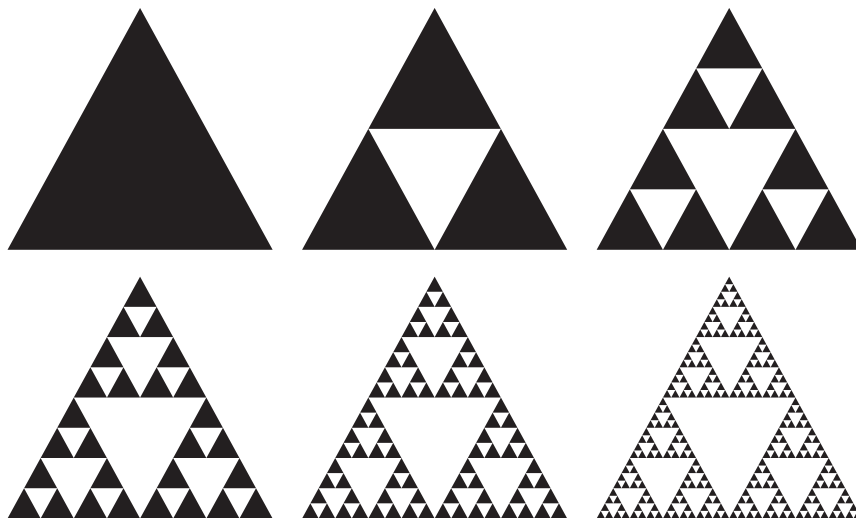

Fig. 8.6 Construction of the Sierpinski triangle in six iterative steps. Each triangle is subdivided into four triangles of half the size, with the middle one taken out. The Hausdorff dimension of the Sierpinski triangle is $D = \log(3)/\log(2) \approx 1.585$.

triangle can directly be calculated with Eq. (8.2.2),

$$D = \lim_{\varepsilon \to 0} \frac{\log n(\varepsilon)}{\log(1/\varepsilon)} = \lim_{i \to \infty} \frac{\log(3^i)}{\log(2^i)} = \frac{\log 3}{\log 2} \approx 1.58496... \,, \qquad (8.2.3)$$

The definition of the Hausdorff dimension (Eq. 8.2.2) leads directly to a practical measurement method. If we grid a 2-D image with a cartesian grid of size $L \times L$, where each macropixel has a size ε, the number of pixels $n(\varepsilon)$ that cover a fractal structure can be directly counted and set into relation with the linear extension of the structure $L = 1/\varepsilon$. If we define the number of pixels that cover a fractal structure as the *area* $A = n(\varepsilon)$, the fractal or Hausdorff dimension D can be obtained by

$$D = \frac{\log n(\varepsilon)}{\log(1/\varepsilon)} = \frac{\log A}{\log L} \; . \qquad (8.2.4)$$

Of course, a structure is only fractal when the same value D holds for a range of spatial resolutions $\varepsilon = 1/L$, so the box-counting has to be repeated for a range of spatial resolutions ε. For pixelized astronomical images with a size of $N_x \times N_x$, such as digital images from a CCD readout, it is often convenient to rebin the image by factors of 2^i, i.e., $\varepsilon = 1, 2, 4, 8, 16, ..., N_x$, which mimics the asymptotic limit $\varepsilon \mapsto 0$ in the definition of Eq. (8.2.3).

Sometimes, the fractal dimension D is also evaluated from the perimeter P or an area A, which is related as,

$$P \propto A^{D/2} \; . \qquad (8.2.5)$$

Note that the perimeter would scale as $P \propto A^{1/2}$ for linear features ($D = 1$), while it scales as $P \propto A$ for area-filling, meandering curves ($D = 2$).

The reader should be cautioned that the fractal dimension measured from a given observation depends very much on the definition of the measurement method. Thus, different computation methods may give differing values. The value of the Hausdorff dimension D (defined with Eq. 8.2.4) does not necessarily need to be identical with the fractal dimension D measured with the perimeter method (defined with Eq. 8.2.5), even when they are measured from an identical data set. Different methods used are specified in Table 8.1 (second column).

We show an example of the determination of the Hausdorff dimension for a solar EUV image recorded during the 1998 July 14 flare in Fig. 8.7 (called the Bastille-Day event because it occurred during the French national holiday). The image is rebinned into macropixels of size $\varepsilon = 1, 2, 4, 8, 16, 32, 64$ and the fractal dimension is determined by counting the macropixels with a brightness above some flux threshold, which yields the values of $D(\varepsilon = 1) = 1.607$, $D(\varepsilon = 2) = 1.563$, ..., $D(\varepsilon = 64) = 1.503$. The mean and standard deviation of the dimension determined with different macropixel sizes is $D = 1.55 \pm 0.03$, so it is approximately constant and thus the structure can be called fractal. A more accurate method would be to obtain D from the graph $\log(n)$ vs. $\log(1/\varepsilon)$ (Eq. 8.2.4).
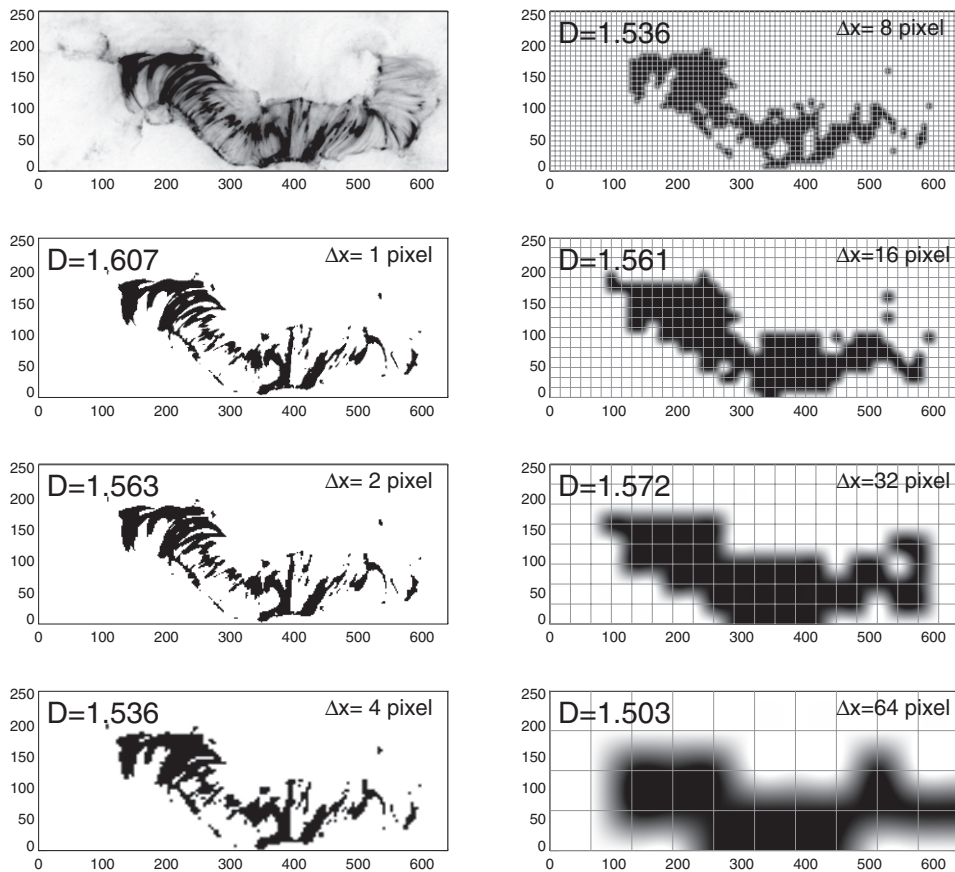
Fig. 8.7 Measurement of the fractal area of the Bastille-Day flare, observed by TRACE 171 Å on 2000-Jul-14, 10:59:32 UT. The Hausdorff dimension is evaluated with a box-counting algorithm for pixels above a threshold of 20% of the peak flux value, with a mean of $D_2 = 1.55 \pm 0.03$ for the 7 different spatial scales shown here. Note that the Hausdorff dimension is nearly invariant when rebinned with different scales (macropixel sizes of $\Delta x = \varepsilon = 1, 2, 4, 8, 16, 32, 64$, indicated with a mesh grid). The original image with full resolution image ($N_x \times N_y = 640 \times 256$ pixels) is shown on a logarithmic greyscale in the top left frame, with a pixel size of $\Delta x = 0.5''$. The fractal dimension $D = \log(A)/\log(L)$ is simply evaluated from the number of rebinned macropixels $A(L)$ above the flux threshold and the rebinned image size $L = \sqrt{N_x \times N_y}/\Delta x$ (Aschwanden and Aschwanden 2008a).

8.2.2 Solar Photosphere and Chromosphere

The solar surface exhibits various features related to the magneto-convection (granulation, meso-granulation, super-granulation, network) or to areas of concentrated magnetic flux (sunspot umbrae, penumbrae, active regions, pores), which all have irregular geometries that have been subjected to fractal analysis (Table 8.1).

Table 8.1 Area fractal dimension D_2 of scaling between length scale L and fractal area $A(L) \propto L^{D_2}$ of various solar phenomena observed in white light, magnetograms, H-α, EUV, and soft X-rays. References: 1, Roudier and Muller (1987); 2, Hirzberger et al. (1997); 3, Bovelet and Wiehr (2001); 4, Paniveni et al. (2005); 5, Janssen et al. (2003); 6, Lawrence (1991); 7, Lawrence and Schrijver (1993); 8, Balke et al. (1993); 9, Meunier (1999); 10, Meunier (2004); 11, Lawrence et al. (1993); 12, Cadavid et al. (1994); 13, Lawrence et al. (1996); 14, McAteer et al. (2005); 15, Gallagher et al. (1998); 16, Georgoulis et al. (2002); 17, Aschwanden and Parnell (2002); 18, Aschwanden and Aschwanden (2008a,b).

Wavelengths regime and phenomenon (reference in superscript)	Method	Area fractal dimension D
Photosphere		
White-light of granules[1]	perimeter area	1.25, 2.15
White-light of granules[2]	perimeter area	1.3, 2.1
White-light of granular cells[2]	perimeter area	1.16
White-light of granules[3]	perimeter area	1.09
Magnetogram super-granulation[4]	perimeter area	1.25
Magnetograms of small scales[5]	perimeter area	1.41 ± 0.05
Magnetograms of active regions[6,7]	linear size area	1.56 ± 0.08
Magnetograms of plages[8]	linear size area	1.54 ± 0.05
Magnetograms of active regions[9]	linear size area	1.78–1.94
	perimeter area	1.48–1.68
Magnetograms of active regions[10]	perimeter area	
− Total		1.71–1.89
− Cycle minimum		1.09–1.53
− Cycle rise		1.64–1.97
− Cycle maximum		1.73–1.80
Magnetograms quiet Sun, active regions[11]	box-counting	multifractal
Magnetograms of active regions[12,13]	box-counting	multifractal
Magnetograms of active regions[14]	box-counting	1.25–1.45
Chromosphere		
EUV of quiet Sun network[15]	box-counting	1.30–1.70
H-α of Ellerman bombs[16]	box-counting	1.4
Corona, Flares		
EUV 171 Å of nanoflares[17]	box-counting	1.49 ± 0.06
EUV 195 Å of nanoflares[17]	box-counting	1.54 ± 0.05
Yohkoh SXT of nanoflares[17]	box-counting	1.65
EUV 171 Å of Bastille-Day flare[18]	box-counting	1.57–1.93

The solar granulation has a typical spatial scale of $L = 1,000$ km, or a perimeter of $P = \pi L \approx 3,000$ km. Roudier and Muller (1987) measured the areas A and perimeters P of 315 granules and found a powerlaw relation $P \propto A^{D/2}$ (Eq. 8.2.5), with $D = 1.25$ for small granules (with perimeters of $P \approx 500$–4,500 km) and $D = 2.15$ for large granules (with $P = 4,500$–15,000 km). The smaller granules were interpreted in terms of turbulent origin, because the predicted fractal dimension of an isobaric atmosphere with isotropic and homogeneous turbulence is $D = 4/3 \approx 1.33$ (Mandelbrot 1977). Similar values were found by Hirzberger et al. (1997). Bovelet and Wiehr (2001) tested different pattern recognition algorithms (Fourier-based recognition technique FBR and multiple-level tracking MLT) and found that the value of the fractal dimension strongly depends on the measurement method. The MLT method yielded a fractal dimension of $D \approx 1.1$, independent of the spa-
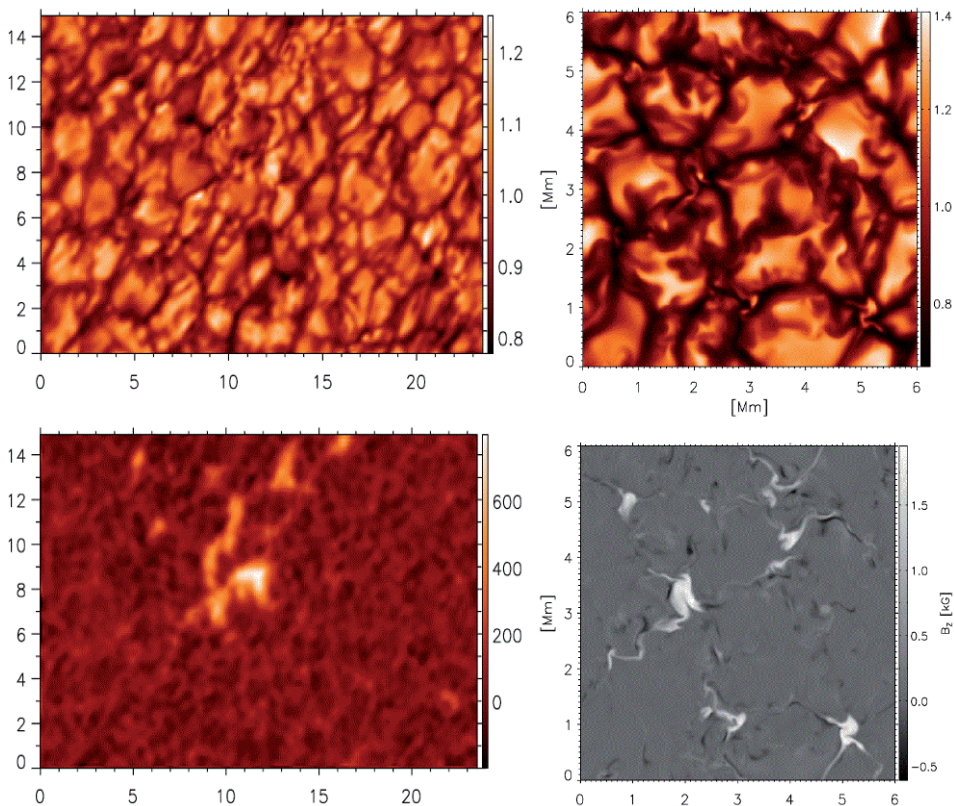
Fig. 8.8 *Left:* A speckle-reconstructed broadband image (top) and magnetogram (bottom) obtained with the Göttingen Fabry-Perot spectrometer at the Vacuum Tower Telescope on Tenerife. Tickmarks are given in arcseconds. *Right:* Snapshot of a numerical simulation of magneto-convection with the MURAM code, tuned to an average vertical field of 50 G. The upper panel shows the frequency-integrated intensity, while the lower panel shows the vertical magnetic field component B_z at a height with opacity $\tau_{5000} = 1$. The pixel size is 21 km, and the full image has a size of 6,000 km. Both the data and the numerical simulations were found to have a very similar fractal dimension of $D \approx 1.4$ (Janssen et al. 2003).

tial resolution, the heliocentric angle, and the definition in terms of temperature or velocity. Meunier (1999) evaluated the fractal dimension with the perimeter–area method and found $D = 1.48$ for supergranular structures to $D = 1.68$ for the largest structures, while the linear size-area method yielded $D = 1.78$ and $D = 1.94$, respectively. In addition, a solar cycle dependence was found by Meunier (2004), with the fractal dimension varying from $D = 1.09 \pm 0.11$ (minimum) to $D = 1.73 \pm 0.01$ for weak-field regions ($B_m < 900$ G), and $D = 1.53 \pm 0.06$ (minimum) to $D = 1.80 \pm 0.01$ for strong-field regions ($B_m > 900$ G), respectively. A fractal dimension of $D = 1.41 \pm 0.05$ was found by Janssen et al. (2003), but the value varies as a function of the center-to-limb angle and is different for a speckle-reconstructed image that eliminates seeing and noise. An example of data and numerical

simulations with a time-dependent magneto-convection code is shown in Fig. 8.8, which both were found to have a very similar fractal dimension.

A completely different approach to measuring the fractal dimension D was pursued in terms of a 2-D diffusion process, finding a fractal diffusion with dimensions in the range of $D \approx 1.3$–1.8 (Lawrence 1991) or $D = 1.56 \pm 0.08$ (Lawrence and Schrijver 1993) by measuring the dependence of the mean square displacement of magnetic elements as a function of time. Similar results were found by Balke et al. (1993), The results exclude Euclidean 2-D diffusion but are consistent with percolation theory for diffusion of clusters at a density below the percolation threshold (Lawrence and Schrijver 1993; Balke et al. 1993).

Fractal dimensions were also evaluated with a box-counting method, finding a range of $D \approx 1.30$–1.70 for chromospheric network structures in a temperature range of $T = 10^{4.5}$ – 10^6 K (Gallagher et al. 1998), a value of $D \approx 1.4$ for so-called *Ellerman bombs* (Georgoulis et al. 2002), which are short-lived brightenings seen in the wings of the Hα line from the low chromosphere, or a range of $D \approx 1.25$–1.45 from a large survey of 9,342 active region magnetograms (McAteer et al. 2005),

The physical understanding of solar (or stellar) granulation has been advanced by numerical convection models and N-body dynamic simulations, which predict the evolution of small-scale (granules) into large-scale features (meso or supergranulation), which is organized by surface flows which sweep up small-scale structures and form clusters of recurrent and stable granular features (Hathaway et al. 2000; Berrilli et al. 2005; Rieutord et al. 2008, 2010). The fractal structure of the solar granulation is obviously a self-organizing pattern that is created by a combination of subphotospheric magneto-convection and surface flows, which is a turbulence-type phenomenon, but is not in a critical state. The fractal structure of magnetic features, however, such as sunspots, active regions, magnetic pores), originate from magnetic flux emergence by buoyancy from the solar interior, which occur at independent places and times, and thus could possibly be attributed to a SOC system. The finding of a fractal dimension in magnetic features thus represents a necessary condition for scale-free (spatial) parameters that is typical for SOC, but not a sufficient condition. If the distributions of lifetimes, peak energies, and total energies of magnetic features also reveal powerlaw distributions, we can consider the driving system, i.e., the solar dynamo at the bottom of the tachocline (in a depth of ≈ 0.3 solar radii below the surface), to operate in a self-organized critical state. Instead of trickling sand grains on top of a SOC sandpile, the solar dynamo generates buoyant magnetic fluxtubes down in the tachocline, which cluster into small or large magnetic filament bundles when bubbling up to the solar surface in an avalanche-like fashion. The question is whether it is a SOC phenomenon or percolation. We will discuss percolation theory in Section 10.6.

8.2.3 Solar Flares

We have already extensively established that solar flares fulfill all criteria of a SOC system, regarding powerlaw distributions of total energies, peak energies, durations (Section 7.3), and waiting-time distributions in terms of a nonstationary Poisson process (Section 5.6).
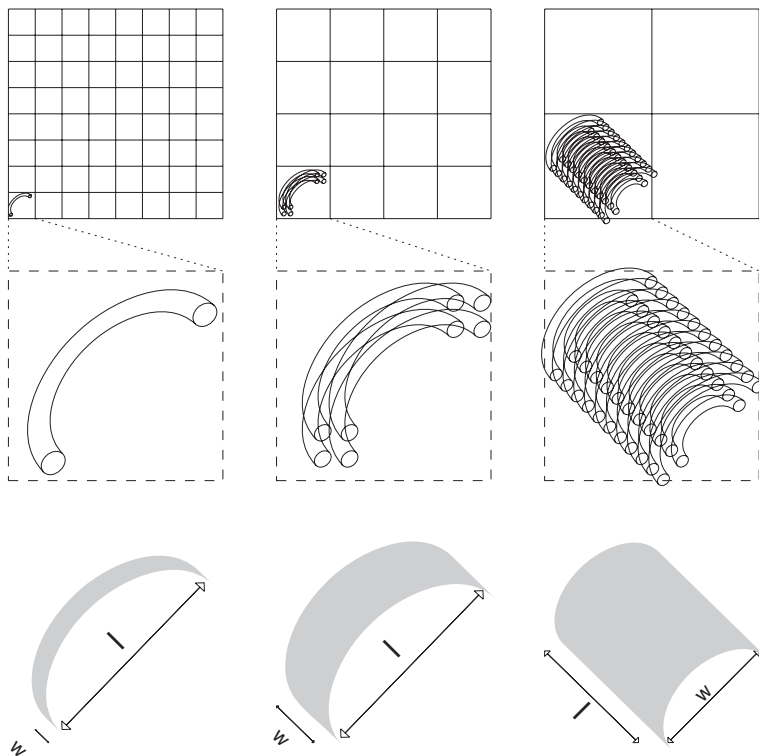
Fig. 8.9 Fractal geometric concept of nanoflares and flares: The cartesian grids (top row) indicate three different spatial resolutions. Flare structures consist of single flux tubes or arcades of multiple flux tubes (middle row) that form fractal contours. The flare area can roughly be estimated from the rectangular area $A = l \times w$ (gray areas in bottom row), regardless of the curvature and composition of the shape. The equivalent width $w = A/l$ provides also a good estimate of the line-of-sight depth according to the geometric single or multi-fluxtube models (middle row) and can be used to estimate the scaling of the volume, i.e., $V = l \times w^2$ (Aschwanden and Parnell 2002).

Consequently we expect also scale-free (powerlaw) distributions of spatial scales (lengths, areas, volumes) with fractal properties.

A fractal geometric concept of a solar flare is shown in Fig. 8.9, which consists of arcades of semi-circular flux tubes that generally are expected to have fractal (i.e., less than solid area-filling) contours above some flux level. For small flares (e.g., nanoflares observed in EUV), the fractal structure may not be resolved even in high-resolution ($\lesssim 1''$) images, but a crude characterization of their projected area A would at least show some asymmetry in their shape, which can be measured from the length l and width w of their elliptical shape (Fig. 8.9, bottom panels). Scaling the width w to the length l with a power-law index b, and characterizing the occurrence frequency distribution $N(l)$ of lengths with a powerlaw index a, we expect the following scaling relations and frequency distributions

for fractal flare areas,

$$
\begin{aligned}
w(l) &\propto l^b \\
l(w) &\propto w^{1/b} \\
A(l) &\propto lw = l^{1+b} = l^D \\
N(l)\, dl &\propto l^{-a}\, dl \\
N(w)\, dw &\propto w^{-[1+(a-1)/b]}\, dw \\
N(A)\, dA &\propto A^{-(a+b)/(1+b)}\, dA
\end{aligned}
\tag{8.2.6}
$$

The corresponding Hausdorff dimension $D = \log(A)/\log(l)$ is

$$
D = (1+b) < 2 ,
\tag{8.2.7}
$$

Data analysis of ≈ 1000 nanoflares observed in EUV (TRACE and soft X-rays (Yohkoh) yielded values of $a = 2.5 \pm 0.2$ and $b = 0.5 \pm 0.2$, which corresponds to a Hausdorff dimension of $D = 1.5 \pm 0.2$ and an area distribution of $N(A) \propto A^{-2.0}$ (Aschwanden and Parnell 2002).

The geometric flare concept shown in Fig. 8.9 visualizes small flares that consist of only one single or a few loops (Fig. 8.9, left and middle), which is typical for EUV nanoflares, but also large flares, which consist of hundreds of loops, geometrically arranged in near-concentric arcades (Fig. 8.9, right). The fractal structure of such large flares has been investigated in detail for the Bastille-Day flare of 2000 July 14 (Aschwanden and Aschwanden 2008a). The story is not simple. Measuring the fractal dimension as a function of time, but normalizing it to the same flare area A_{max} defined around the peak time of the flare, the fractal area varies in the range of $A(t)/A_{max} = 0.08$–0.67, corresponding to a Hausdorff dimension of $D(t) = 1.57$–1.93. The time evolution is shown in Fig. 8.10, which exhibits some correlation of the fractal dimension with the EUV flux, which essentially tells us that more and more fractal structures (flare loops) brighten up before the flare peak. Typically, a flare starts when a first loop brightens up, which is a nearly linear feature and thus has a dimension of $D \gtrsim 1$, while more and more loops come into play as the flare progresses, until the flare area is almost solidly filled with $D \lesssim 2$. Moreover, the determination of the fractal dimension depends also on the flux threshold. Data as well as simulations show a variation of the fractal dimension of $D \approx 1.4$–1.9 depending on the chosen flux threshold, say in the range of $F_{th} = 10$–50 DN s^{-1} as shown in Fig. 8.11. Generally, the value of the fractal dimension drops with higher thresholds. In the same study, a total of 20 large (GOES X-class and M-class) flares were investigated from TRACE observations, which all have very complex fractal finestructure, as shown in Fig. 8.12, and the fractal dimensions cover a substantial range during the flare evolution. A summary of the fractal areas ranges $A(L)$ versus the length scale L is shown in Fig. 8.13, which has a mean fractal dimension of $D = 1.89 \pm 0.05$ during the flare peak, but covers a range of lower values of $D \gtrsim 1.0$–1.5 at the beginning of the flare. Thus, a complete SOC theory should also include the time evolution of the fractal geometry. Our simplest SOC work model (Section 3.1) quantifies a SOC avalanche in terms of an exponential growth phase and a linear decay phase, which implies a multiplicative pattern in energy release and spatial structures. In order to predict the temporal evolution of the 2-D fractal dimension, the 3-D evolution of spatial structures has to be mapped into a 2-D plane (see Section 8.3).
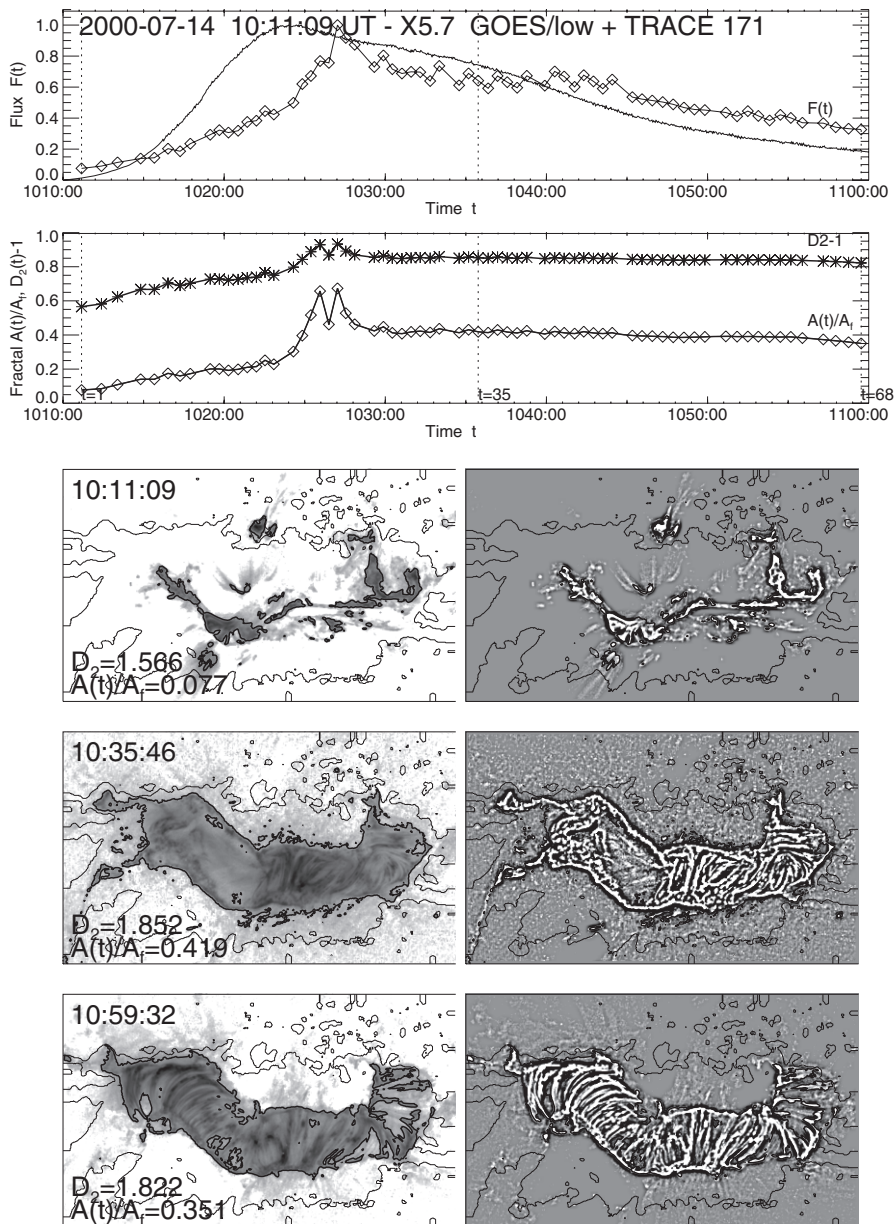
Fig. 8.10 The time evolution of the normalized EUV 171 Å flare flux $F(t)$ (diamonds) and soft X-ray flux from GOES (smooth curve) are shown for the Bastille-Day flare (top panel), along with the fractal area $A(t)/A_f$ and fractal dimension $D_2(t)$ (second panel). The TRACE 171 Å images at start (t_1), middle (t_{35}), and end time (t_{68}) are shown in the three lower panels on a logarithmic flux scale (three lower left panels) and high-pass filtered (three lower right panels). The instantaneous flare areas $A(t)$ are marked with thick black contours, while the time-integrated flare area A_f is marked with thin contours (Aschwanden and Aschwanden 2008a).
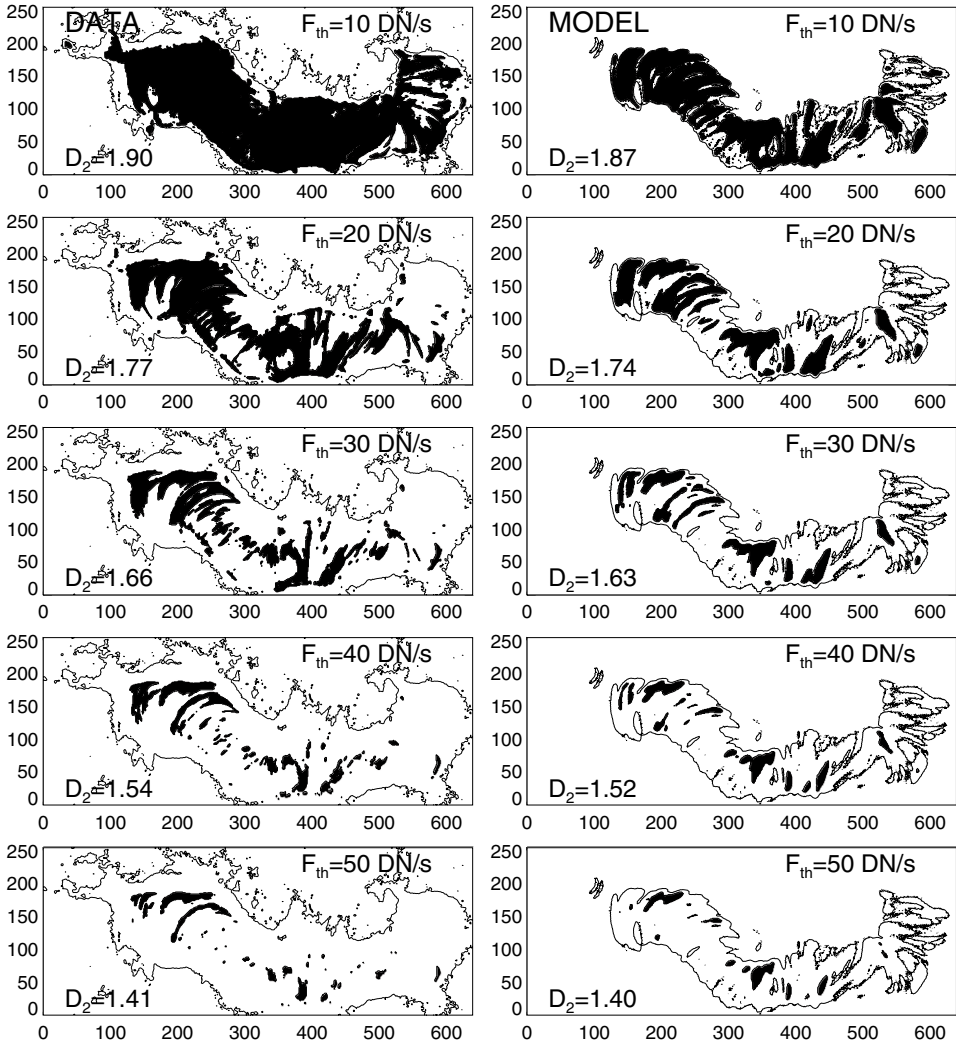
Fig. 8.11 The fractal area $A(F > F_{th})$ is shown for the same data image (left panels) and model image (right panels) as given in Fig. 8.10 for different flux thresholds $F_{th} = 10, 20, ..., 50$ DN s^{-1}. The flare area is contoured at a flux threshold of $F_{th} = 5$ DN s^{-1}. Note the similar dependence of the fractal dimension D_2 (indicated at bottom left corner of each panel) on the flux threshold for data and model (Aschwanden and Aschwanden 2008a).
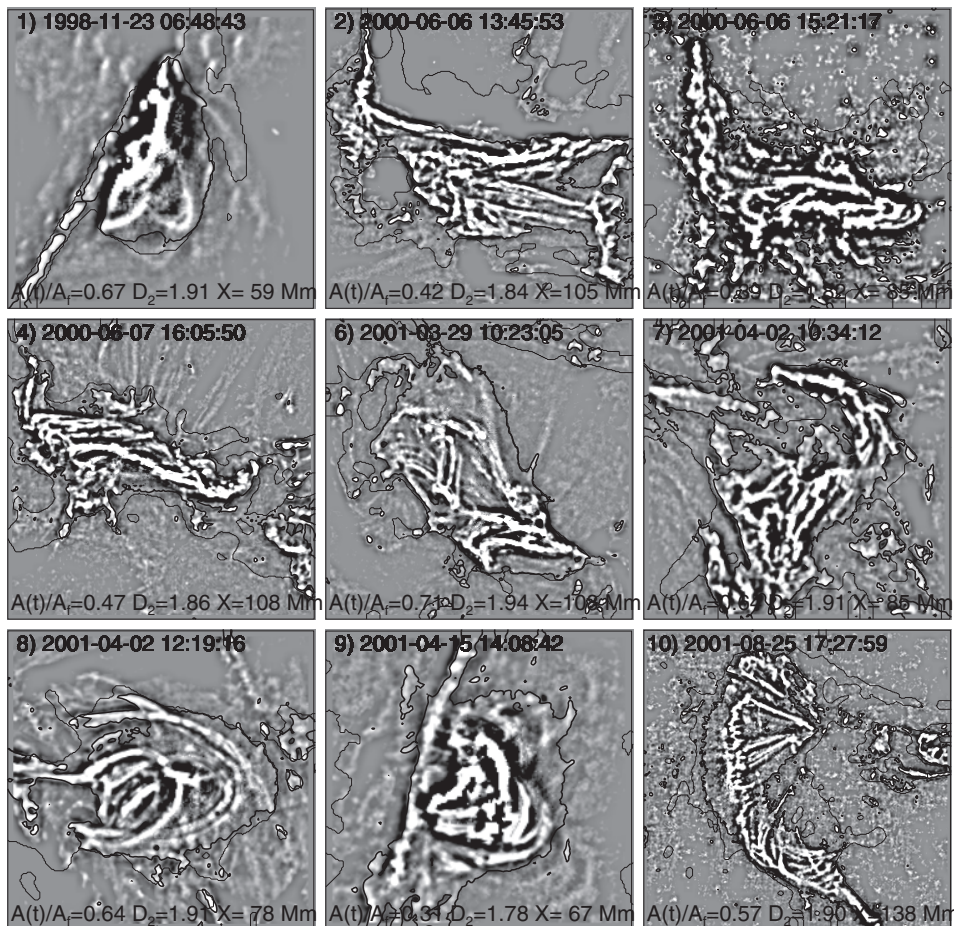
Fig. 8.12 Highpass-filtered images of nine X-class flares are shown, which enhance the fractal finestructure of flare loops (Aschwanden and Aschwanden 2008a).

8.3 3-D Fractals

The theoretical extension of 2-D to 3-D fractal dimension is straightforward. In the definition of the Hausdorff dimension we have to replace the area A by the volume V, and the number $n(\varepsilon)$ of elements that cover a fractal structure are 3-D voxels, rather than 2-D pixels,

$$D_V = \lim_{\varepsilon \mapsto 0} \frac{\log n(\varepsilon)}{\log(1/\varepsilon)} = \frac{\log V}{\log L} \ . \tag{8.3.1}$$

The practical measurement of a 3-D fractal dimension D_V, however, is not straightforward, but can be inferred with help of tomographic 2-D projections and computer simulations. Especially in astrophysical applications, only 2-D data are available in general, and thus
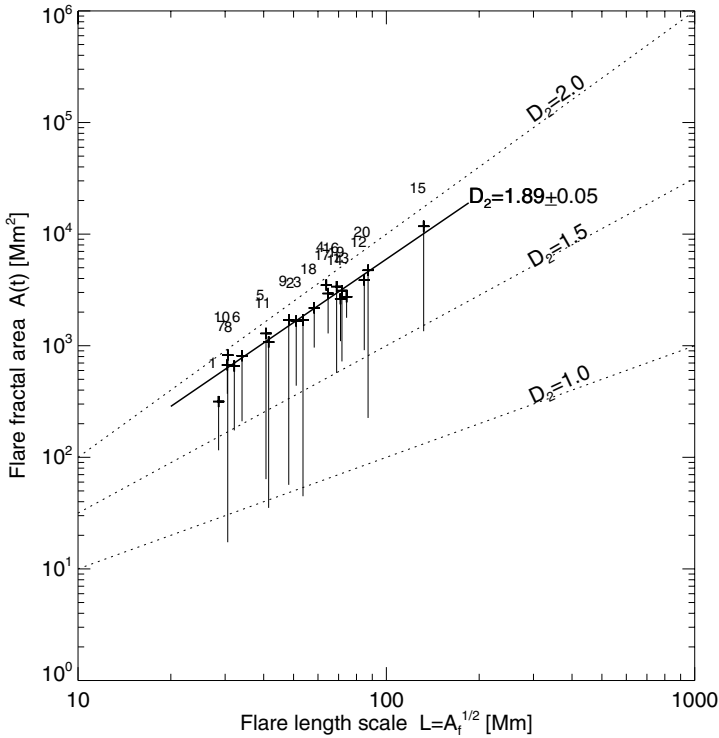
Fig. 8.13 Fractal areas $A(t)$ of flares as a function of the spatial length scale $L = \sqrt{A_f}$. For each flare there is an evolution of the fractal area $A(t)$ as a function of time (vertical range). The cross symbols mark the maximum of the fractal dimension reached during the entire flare duration. The fractal dimensions of $D_2 = 1.0, 1.5, 2.0$ are indicated with dotted lines, and the average maximum fractal dimension D_2 is indicated with a thick solid line, having a mean of $D_2 = 1.89 \pm 0.05$ (Aschwanden and Aschwanden 2008a).

the inference of a 3-D fractal dimension requires a spatial model, stereoscopic observations, or tomographic reconstructions. The scale invariance in terms of 3-D fractal geometry, however, has been probed from microscopic structures such as snow crystals (e.g., Westbrook et al. 2004), all the way to clustering of galaxies, cosmic voids, and dark matter (e.g., Gaite 2007).

8.3.1 Cellular Automaton Simulations

Cellular automaton simulations of SOC models have generally been performed in both 2-D and 3-D geometries (e.g., Bak et al. 1987, 1988; Lu and Hamilton 1991; Charbonneau et al. 2001). Special attention to the relationship between the 2-D and 3-D fractal dimension has been paid in the studies of Charbonneau et al. (2001), McIntosh and Charbonneau (2001), and McIntosh et al. (2002). An example of a 3-D avalanche with 2-D projections in a cellular automaton run is shown in Fig. 8.14. For their largest simulated datacubes
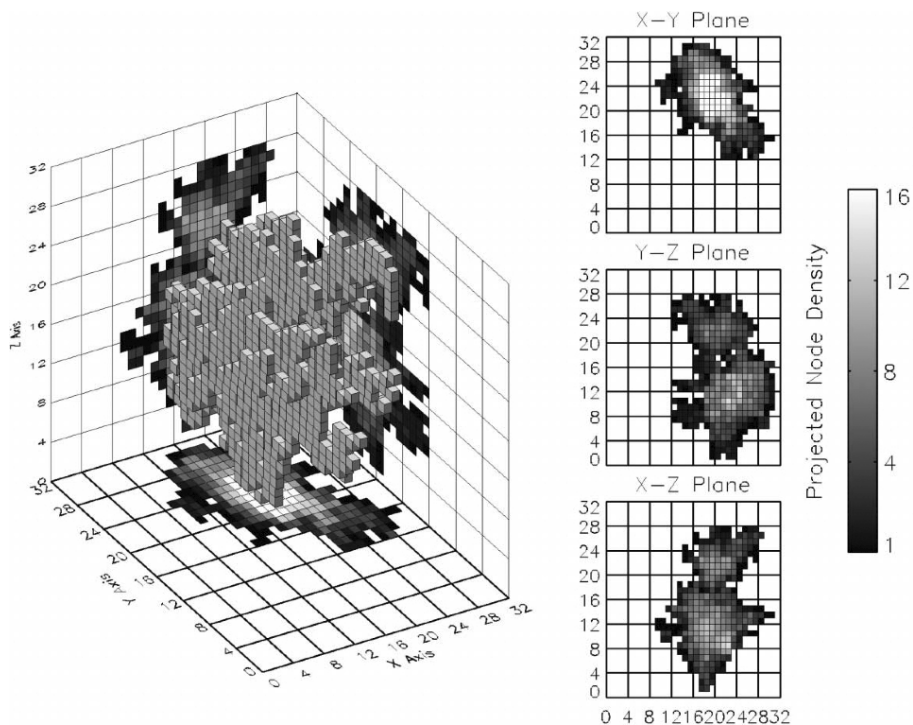
Fig. 8.14 The 3-D structure of a time-integrated avalanche in a 32^3 lattice. The 2-D projections of the avalanche are shown separately in the right-hand panels, with the gray-scale indicating the number of avalanching nodes, which corresponds to the column depth along the line-of-sight in astronomical observations (McIntosh and Charbonneau 2001; reproduced by permission of the AAS).

($N^3 = 64^3$), they obtained a relationship,

$$V(A) \propto A^{1.41 \pm 0.04} \ , \tag{8.3.2}$$

while the Euclidean scaling would be $V \propto A^{3/2}$, so the relationships are not identical for fractal and solid bodies.

There are different ways to define the linear size L of a fractal structure. One method is to define a *radius of gyration R*,

$$R^2 = \frac{1}{M} \sum_{i=1}^{M} |\mathbf{r}_i - \mathbf{R}_0|^2 \ , \tag{8.3.3}$$

where the sum runs over the M nodes that are part of the avalanche cluster, and $\mathbf{R}_0 = (1/M) \sum \mathbf{r}_i$ is the cluster's center of mass. Physically, R is the radius of the thin spherical shell (circular ring in 2-D) that has the same "mass" and moment of inertia as the original cluster (Stauffer and Aharony 1994; Charbonneau et al. 2001). Using this definition for the length scale ($L = R$), Charbonneau et al. (2001) find the following scaling for their

simulation with the largest 3-D cube ($N^3 = 128^3$),

$$A(L) \propto L^{1.78 \pm 0.02} \, , \tag{8.3.4}$$

while the Euclidean scaling would be $A \propto L^2$. Combining these two fractal scaling laws (Eqs. 8.3.2 and 8.3.4) we infer the relationship between the fractal volume V and the length scale L,

$$V(L) \propto L^{2.51 \pm 0.06} \, , \tag{8.3.5}$$

which also differs from the Euclidean scaling $V \propto L^3$. Of course, these scaling laws apply to the particular setup of cellular automaton models we described in Chapter 2, but slightly different values are expected for different avalanche models or length scale definitions. We have also to be aware that these simulated fractal structures (as shown in Fig. 8.14) represent time-integrated structures, while the fractal dimensions of instantaneous snapshots are generally smaller.

8.3.2 Solar Flares

Since geometric 3-D models of solar flares are unavoidable in calculating electron densities and thermal energies from the observed volume-integrated emission measures in soft X-rays and EUV, which are necessary parameters to infer occurrence frequency distributions of flare energies for SOC models, the 3-D fractal dimension D_V is a fundamental parameter. Alternatively, one can specify a volume-filling factor q_V, which is the ratio of the fractal V to the Euclidean volume V_0,

$$q_V = \frac{V}{V_0} = \frac{L^{D_V}}{L^3} = L^{D_V - 3} \, , \tag{8.3.6}$$

while the area-filling factor q_A can be defined analogously in terms of the area fractal dimension D_A,

$$q_A = \frac{A}{A_0} = \frac{L^{D_A}}{L^2} = L^{D_A - 2} \, . \tag{8.3.7}$$

Based on the geometric concept of flares introduced in Fig. 8.9, we can construct a volumetric model in terms of an arcade that contains a variable number of concentric half loops that fill the half-cylindric volume to some extent, parameterized by the arcade length l_a, arcade width w_a, and average loop width w_{loop}. While the 3-D volume is invariant to rotation, the projected area will depend on the aspect angle, longitude, or center-to-limb distance, as shown in Fig. 8.15. If we allow for fractal filling with n_{loop} loop structures, which has the limit of $n_{loop}^{max} \approx l_a w_a / 2 w_{loop}^2$ for the arcade model shown in Fig. 8.15, one can derive the following geometric filling factors (Aschwanden and Aschwanden 2008b),

$$q_V = \frac{n_{loop}}{n_{loop}^{max}} = n_{loop} \left(\frac{2 w_{loop}^2}{l_a w_a} \right) \, . \tag{8.3.8}$$
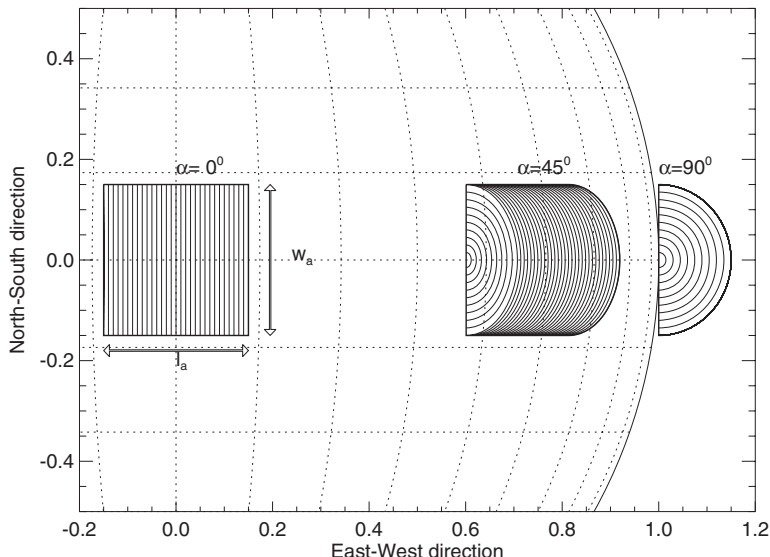
Fig. 8.15 The geometry of a semi-cylindrical flare arcade model is shown, quantified by the arcade length l_a in the east–west direction, the arcade width w_a in the north–south direction, and the line-of-sight angle α to the solar vertical (or relative longitude difference to solar disk center). The three cases correspond to $\alpha = 0°, 45°, 90°$ with an aspect ratio of $w_a/l_a = 1$. The total (Euclidean) flare area is outlined in thick linestyle, while the loop quantization is indicated with thin lines (Aschwanden and Aschwanden 2008b).

$$q_A = \frac{A(n_{loop})}{A_0} = \left[1 - \exp\left(-n_{loop}\frac{A_1}{A_0}\right)\right] , \tag{8.3.9}$$

where A_1 is the Euclidean area that depends on the aspect angle α,

$$A_1(\alpha) \approx w_{loop}\frac{w_a}{2}\left[1 + \left(\frac{\pi}{2} - 1\right)\sin^{3/2}(\alpha)\right] . \tag{8.3.10}$$

Using the definitions of Eqs. (8.3.6) and (8.3.7), the area and volume fractal dimensions can then be calculated from the area- and volume-filling factors,

$$D_V = 3 + \frac{\ln q_V}{\ln L} . \tag{8.3.11a}$$

$$D_A = 2 + \frac{\ln q_A}{\ln L} . \tag{8.3.11b}$$

where the length scale L can be defined from the Euclidean volume V_0,

$$V_0 = \frac{\pi}{2}\left(\frac{w_A}{2}\right)^2 l_a , \tag{8.3.12}$$
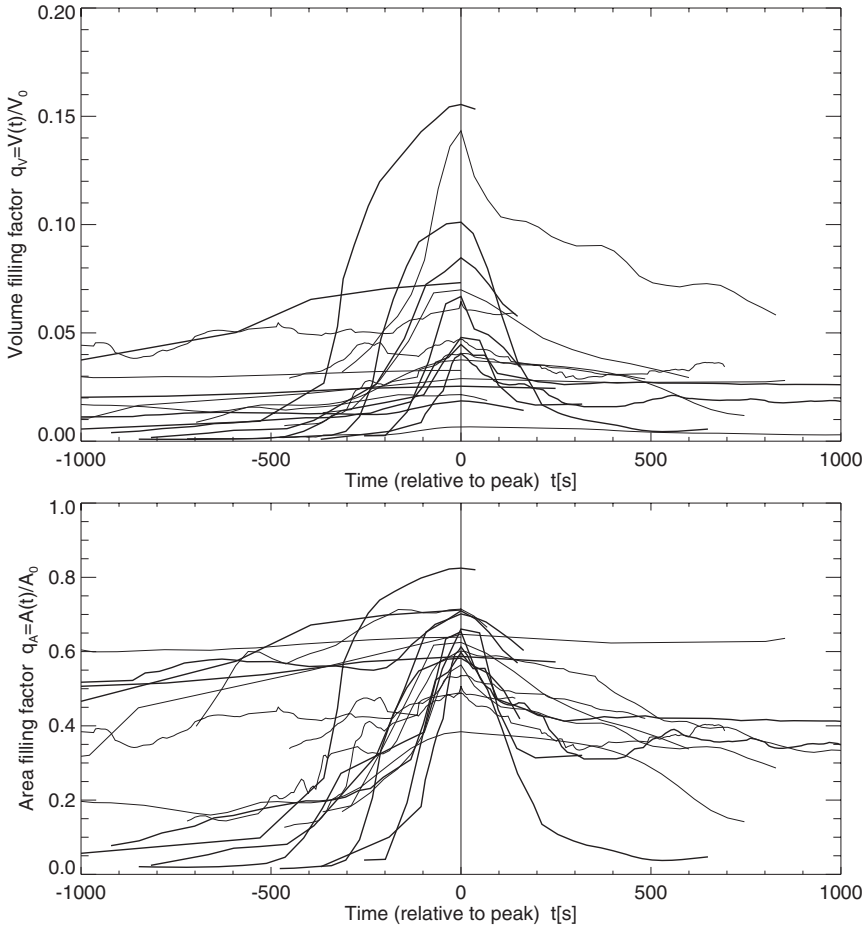
$$L = V_0^{1/3} . \tag{8.3.13}$$

Fig. 8.16 The area-filling factor $q_A(t)$ (bottom panel) and the inferred volume-filling factor $q_V(t)$ (top panel) are shown for 20 flares, as a function of the time relative to the peak in the maximum fractal area. Flares which have an increase of more than 0.5 in the fractal area during the rise time are outlined with thick linestyle. Note that maximum area-filling factors do not exceed 0.8, while maximum volume-filling factors do not exceed 0.15 (Aschwanden and Aschwanden 2008b).

We have already shown how the observed area fractal dimension varies as a function of time during a flare (Fig. 8.10), and consequently also the area- and volume-filling factors do. In Fig. 8.16 the results of the time evolution of flare-filling factors q_A and q_V are shown for 20 large flares, varying typically in the range of $q_V \approx 0.001$–0.03 at flare start, $q_V \approx 0.03$–0.08 at flare peak, and $q_V \approx 0.01$–0.06 at flare end. These filling factors are very important, because they constrain the true mean electron density n_e. If an average electron density $\langle n_e \rangle = \sqrt{EM/V_0}$ is estimated for a unity filling factor (solid filling of the flare volume), the correct mean electron density in the fractal flare volume scales as.

$$n_e = \sqrt{EM/V} = \langle n_e \rangle \sqrt{V_0/V} = \langle n_e \rangle \sqrt{1/q_V} \,. \tag{8.3.14}$$

This correction is important in deriving correct thermal energies of flares,

$$E_{th} = \int 3n_e(T)k_B T V(T) \, dT \approx 3n_e k_B T_e V = \frac{3k_B EMT_e}{n_e} \,, \tag{8.3.15}$$

where EM is the total emission measure, T_e the electron temperature, and n_e the electron density at the peak time of the flare.

8.4 Multifractal Analysis

The geometric concepts we described so far are all *monofractal*, which contain self-similar and scale-invariant structures that can be characterized by a single fractal dimension, such as the Hausdorff dimension D. However, there is no structure in the universe that exhibits the same fractal dimension at all scales from the microscopic to the macroscopic limit. Geometric structures are generated by different physical processes that operate within a preferred scale range each, and thus the resulting structures have a different degree of inhomogeneity or fractality at different scales. The concept of *multifractals* attempts to characterize the degree of geometric complexity with multiple scaling exponents or fractal dimensions, which in the continuum limit results into a spectrum of fractal dimensions. While the fractal dimension D is defined by $n(\varepsilon) \approx \varepsilon^{-D}$ for monofractals in the framework of the box-counting method (Eq. 8.2.2), there is a spectrum $f(\alpha)$ of exponents for multifractals, also called *singularity spectrum*,

$$n(\varepsilon) \propto \varepsilon^{-f(\alpha)} \,, \tag{8.4.1}$$

where α is the relative strength or significance. Examples of the singularity spectrum $f(\alpha)$ are shown in Fig. 8.17 for a monofractal (Sierpinski carpet with Hausdorff dimension $D = log(8)/log(3) \approx 1.89279$), for a theoretical multifractal image (Cadavid et al. 1994), and for observational data from solar magnetogram data (Hewett et al. 2008; Conlon et al. 2008). The latter example shows a typical singularity spectrum, which has a peak of $f(\alpha)_{max}$ and a minimum of $f(\alpha)_{min}$, which is also characterized by the terms *contribution diversity* $C_{div} = \alpha_{max} - \alpha_{min}$ and *dimensional diversity* $D_{div} = f(\alpha)_{max} - f(\alpha)_{min}$, both being measures of the geometric complexity and richness of a fractal structure. Related measures of complexity are also multiscaling of Kadanoff and Lipshitz–Hölder exponents (e.g., see Georgoulis et al. (1995) and references therein).

The magnetic field seen at the solar surface reveals a richness of morphological structures that are termed sunspots, plages, network, intranetwork, magnetic knots and pores, etc. A quiet-Sun photospheric magnetogram was first analyzed in terms of multifractal analysis by Lawrence et al. (1993), who modeled the singularity spectrum with a Gaussian random process. More detailed modeling was done by Cadavid et al. (1994) by adding Gaussian white noise to theoretical self-similar and multifractal structures, finding that the degree of multifractality is enhanced for more intermittent distributions and strong correlations between cells. The influence of finite spatial resolution on the determination of multi-
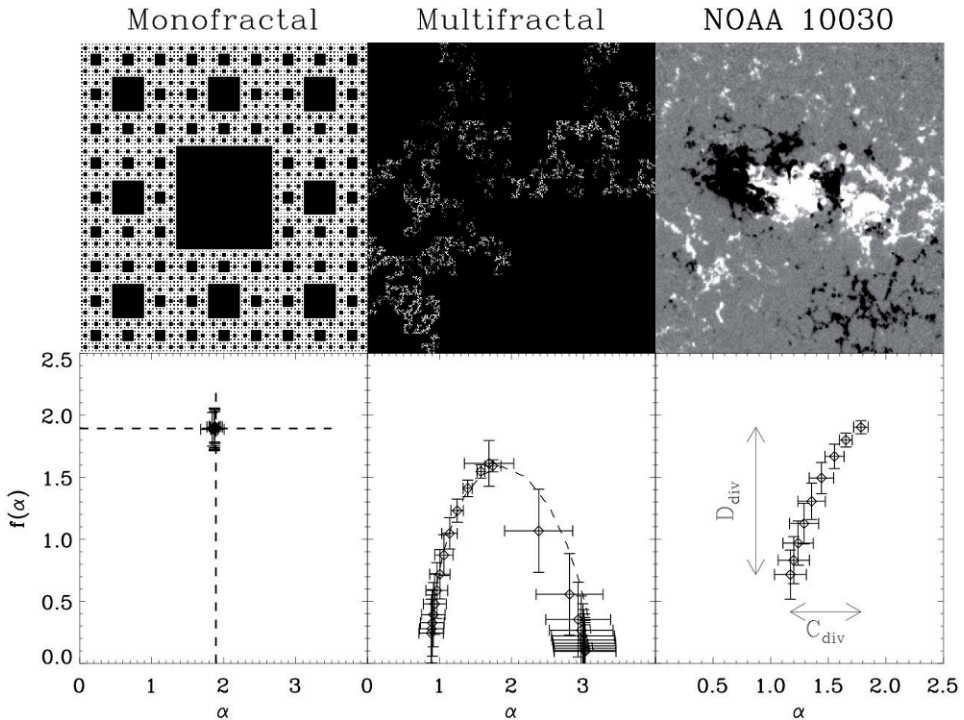
Fig. 8.17 A monofractal image of the Sierpinski carpet (left), a theoretical multifractal image (middle), and an observed multifractal solar magnetogram of active region NOAA 10030 (right), along with the singularity spectra $f(\alpha)$ (bottom panels) determined for these structures (Conlon et al. 2008).

fractal scaling was investigated by Lawrence et al. (1996) who found that the box-counting method is unreliable if it does not fill the embedding Euclidean dimension ($D < 2$). The multifractal singularity spectrum was also applied in time sequences of photospheric magnetograms to study the evolution of active regions (Conlon et al. 2008), see a snapshot in Fig. 8.17. It was found that active regions that evolved into large-scale coherent structures show a decrease of dimensional diversity D_{div}, and a relationship was found between the flaring rate in an active region and the multifractal properties (Conlon et al. 2008). The multifractal complexity was also found to vary as a function of the solar cycle, or between the northern and southern hemisphere (Sen 2007).

Multifractal analysis appears to be a sensitive tool for characterizing complexity and changes in complexity of spatial morphological structures, either as a function of space, or as a function of time, similar to the Bayesian statistics of nonstationary Poisson processes used in the time domain (Section 5.2).

Another multi-scale method that is related to multifractal analysis is the *structure function*, which has been developed to describe the statistical behavior of fully developed turbulence (Kolmogorov 1941). Structure functions express the degree of correlation at different length scales, equivalent to the correlation function of velocity fluctuations as a function

of the spatial distance, which has a similar scaling behavior as the singularity spectrum of a multifractal structure. The scaling behavior of structure functions has been studied in magnetograms of the solar photosphere (Abramenko et al. 2002, 2003; Abramenko 2005), revealing significant changes of the structure function before and during solar flares, similar to the evolutionary changes of the multifractal singularity spectrum measured for active regions (Conlon et al. 2008).

8.5 Spatial Power Spectrum Analysis

A more traditional multi-scale method is the *spatial 2-D Fourier power spectrum* of a 2-D spatial image, which quantifies the correlated intensity as a function of spatial scales. If we take an image with a size of $N \times N$ pixels and denote the image coordinates with the indices (n,m), the intensity of a particular pixel is $I_{n,m}$. 2-D power spectra I_k (with complex Fourier coefficients) can then be calculated (e.g., Gomez et al. 1993a),

$$I_k = \sum_{n=1}^{N} \sum_{m=1}^{N} I_{n,m} \exp\left[\frac{2\pi i}{N}(nn' + mm')\right] , \qquad (8.5.1)$$

where the Fourier component or wave vector $(k = 2\pi/\lambda)$ in the (k_x, k_y) plane is,

$$k = \frac{2\pi}{N\Delta x}(n', m') , \quad n', m' = 0, 1, ..., (N-1) , \qquad (8.5.2)$$

and Δx is the linear pixel size. The 2-D power spectrum $P(k_x, k_y)$ is then defined as

$$P(k_x, k_y) = \left(\frac{\Delta x}{2\pi}\right)^2 |I_k|^2 . \qquad (8.5.3)$$

An example of such a 2-D Fourier power spectrum of a solar image recorded in soft X-ray wavelengths is shown in Fig. 8.18. The presence of a broad-band spectrum (in contrast to a δ-function peak for non-fractal large-scale spatial structures) indicates spatial structures over a large scale range, down to the image resolution Δx. From the 2-D power spectra, 1-D omnidirectional power spectra can be computed, which average the spectra in all radial directions. Such omnidirectional Fourier spectra have been found to scale with $P(k) \propto k^{-3}$ for some solar active regions (Martens and Gomez 1992; Gomez et al. 1993a), which was explained in terms of a turbulent Kolmogorov spectrum $P(k) \propto k^{-5/3}$, combined with the spectral modifications resulting from the velocity distribution of photospheric granulation and the emission mechanism observed in soft X-rays (Gomez et al. 1993b).

Power spectra analysis in other regions of the solar surface and in other wavelengths were performed in a number of studies. The power spectra are very wavelength-dependent. In the quiet Sun, power spectra of $P(k) \propto k^{-2.7}$ were measured in soft X-rays (Benz et al. 1997), and $P(k) \propto k^{-2.5}$ in EUV Fe XII (Berghmans et al. 1998). Power spectra derived from photospheric magnetograms, after correction for the seeing (modulation transfer function), yielded $P(k) \propto k^{-1}$ for the photospheric network, $P(k) \propto k^{-3.5}$ for the non-
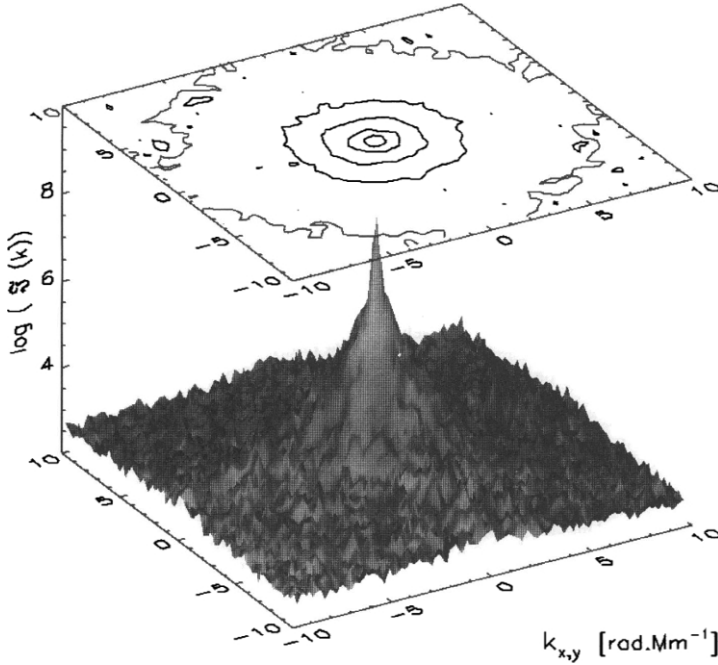
Fig. 8.18 2-D Fourier power spectrum of a soft X-ray image of a solar active region recorded with the *Normal Incidence X-ray Telescope (NIXT)* telescope during a rocket flight in 1989, with a spatial resolution of $0.75''$. The 2-D power spectrum is nearly isotropic (Gomez et al. 1993a; reproduced by permission of the AAS).

network (Lee et al. 1997), $P(k) \propto k^{-1.7}$ for active regions, and $P(k) \propto k^{-1.3}$ for quiet-Sun regions (Abramenko et al. 2001). Observations in extreme ultraviolet, which probe the lower corona rather than the photosphere, yield power spectra of $P(k) \propto k^{-2.0}$ for bright points, $P(k) \propto k^{-2.1}$ for loops, $P(k) \propto k^{-1.9}$ for the background corona, $P(k) \propto k^{-1.6}$ for dark lanes (network), while power spectra in the transition region (in the He II line) yield values of $P(k) \propto k^{-1.5}$ for the same structures (Berghmans et al. 1998). Similar power spectra were measured for full-Sun images in EUV, $P(k) \propto k^{-1.57}$ in the S VI (933 Å) and $P(k) \propto k^{-1.74}$ in the S VI (944 Å) (Buchlin et al. 2006). Power spectra measured with a highest resolution of $0.1''$ (70 km on the solar surface) in the G-band were found to be as steep as $P(k) \propto k^{-4.0}$ in sunspot penumbrae, and $P(k) \propto k^{-3.6}$ in active granulation (Rouppe Van der Voort et al. 2004).

The variety of power spectra measured in solar data reflects a number of effects that affect the precise value of the slope: (1) the physical mechanism (e.g., MHD turbulence in subphotospheric granulation cells), (2) the wavelength of the observer (optical, EUV, soft X-rays), which mostly indicates different altitude levels (photosphere, chromosphere, transition region, corona), and (3) instrumental effects (seeing and spatial resolution). The powerlaw index p of a spatial power spectrum $P(k) \propto k^{-p}$ can be transformed into a distribution of spatial length scales $N(L)$ with $k = 2\pi/L$, with a similar formalism as we derived

in Section 4.8.4 in the time domain. However, there are also other methods to measure the distribution $N(L)$ of length scales directly, as we describe in the next Section 8.6.

8.6 Statistics of Spatial Scales

The common denominator of fractal structures with SOC theory is the property of scale-free parameter ranges, which can be described with powerlaw relations between various geometric parameters (e.g., length, area, volume). The fractal property implies two important consequences for SOC theory: (1) it describes the geometry of the instantaneous internal microstructure of a SOC event, but also (2) describes the relationships of geometric size parameters between different SOC events. The two relationships may even influence each other during a SOC event. For instance, a landscape has a fractal structure as a static property, but leaves an imprint of its static fractality also on dynamic events, such as landslides, flooding, or show avalanches, which follow the channeling and ducting of the fractal terrain. Fractal landscapes (valleys, craters) may even be the witnesses of SOC-like processes (erosion, mountain slides, volcanic eruptions). Solar flares are magnetic reconnection events that occur in the environment of a fractal magnetic field, and thus the resulting energy of a magnetic instability released in a flare, which heats up chromospheric plasma and redistributes it throughout coronal fluxtubes, reflects a similar fractality as the previous static magnetic field. So, we can interpret the fractal geometry of static structures as ducts or remnants of dynamical SOC events, which exhibit the multiplicative imprints of exponentially-growing catastrophes. It is like the domino effect, where an avalanche chain reaction takes place in a pre-arranged fractal geometry.

   In the following we focus on the second consequence of fractal geometries, namely the statistics of spatial size scales between different events. If the main SOC parameters we used so far (i.e., the peak energy P, the total (time-integrated) energy E, and the duration T) possess powerlaw frequency distributions, and if there is a simple powerlaw scaling law of the SOC parameters (P, E, T) with length scales L, we expect also occurrence frequency distributions $N(L)$ of length scales to exhibit a powerlaw-like functional form (Section 7.1.6). Hence, we study the length scale frequency distributions $N(L)$ for different astrophysical SOC processes in the following.

8.6.1 Solar Photosphere and Chromosphere

As we alluded to in previous sections on the (multi)fractal structure of magnetic structures seen on the solar surface and in the solar atmosphere, there is the notion that the internal solar dynamo is the driver and generator of magnetic features (sunspots, active regions, filaments, flares, coronal mass ejections), and thus could represent a dissipative nonlinear system in the state of self-organized criticality (in contrast to turbulence or percolation theories). The static magnetic features seen on the solar surface represent then the remnants of buoyant magnetic fluxtubes generated by the SOC state of the tachocline on one hand, while dynamic magnetic reconnection processes in the solar corona represent a secondary SOC process generated by the SOC state of the solar atmosphere on the other hand.

Early statistics (before SOC) on the distribution of the most prominent magnetic features on the solar atmosphere, namely active regions, was obtained by measuring the areas of over 1,000 active regions during 1967–1981 in daily magnetograms from the Mount Wilson Observatory, detected above a threshold of 10 G. The resulting area size distribution with sizes of $A = 3$–1,350 square degrees (1 square deg = 48.5×10^{-6} of the solar hemisphere), were found to fit an exponential distribution of $N(A) \propto \exp(-A/175)$ (Tang et al. 1984). A more extended study was conducted by Harvey and Zwaan (1993), which differed from the study of Tang et al. (1984) in several ways: (1) only bipolar regions that reach their peak size on the visible hemisphere were included, (2) regions are included only once, (3) each region was measured during the peak, and (4) corrections for visibility and data gaps were made. The resulting size distribution was characterized by a sum of exponential and logarithmic terms and was much different from the one obtained by Tang et al. (1984), but agreed in the invariance of the functional shape during the solar cycle. The size distribution of sunspots sampled over more than 100 years (from Greenwich Observatory 1874–1976) was found to follow a log-normal distribution (Baumann and Solanki 2005), which is powerlaw-like at the upper end, but exhibits a gradual flattening towards smaller sizes. Statistics on areas of magnetic features depend very much on the selection (active regions, sunspots, emerging bipoles), the time evolution (growth, peak, or decay phase), and the counting method (daily records, multiple countings per solar rotation). Moreover, since the total available magnetic energy per feature depends on both the area and the field strength, statistics on areas alone may not be most useful.

An area-related quantity is the magnetic flux $\Phi = \int B \, dA \approx BA$, which includes the magnetic field strength B and is largely independent on the instrumental resolution, because it represents a spatial integral. However, the relationship between the magnetic flux $\Phi \approx BA$ and the area A is not simple and seems to vary in an active region on time scales of days (Chumak and Zhang 2003). Statistics on the distribution of magnetic field strengths in the range of $B = 0$–1,800 G has been quantified in Dominquez Cerdena et al. (2006), which depends very much on the instrumental resolution and whether the Zeeman signal tends to cancel opposite polarization. A powerlaw-like distribution of magnetic fluxes was found for intranetwork (with a slope of $\alpha \approx 1.68$) and network flux (with a slope of $\alpha \approx 1.27$) in the a range of $\Phi \approx 10^{16}$–10^{18} Mx (Wang et al. 1995; Meunier 2003). A series of studies was conducted (Hagenaar et al. 1997, 2003; Hagenaar 2001; Hagenaar and Shine 2005) on the statistical distribution of cell sizes in the chromospheric network, ephemeral magnetic regions, and moving magnetic features around sunspots, and synthesized the different statistics into a single composite powerlaw-like distribution function that contains the magnetic fluxes of emerging bipoles at the lower end and entire active regions at the upper end, spanning a range of about four orders of magnitude ($\Phi \approx 5 \times 10^{18} - 5 \times 10^{22}$ Mx), shown in Fig. 8.19 (left). Parnell et al. (2009) used a "clumping algorithm" and extended this way the range of magnetic fluxes over about seven decades and found that the synthesized distribution of all magnetic features in the range of $\Phi = 10^{16} - 10^{23}$ Mx fit a powerlaw distribution with a slope of $\alpha \approx 1.85 \pm 0.14$ (Fig. 8.19, right). The statistical distributions of magnetic fluxes in active regions has been modeled in terms of percolation models (Wentzel and Seiden 1992; Seiden and Wentzel 1996; Fragos et al. 2004). We will discuss physical SOC models that involve the observed size distributions of magnetic areas and magnetic fluxes in Chapter 9.
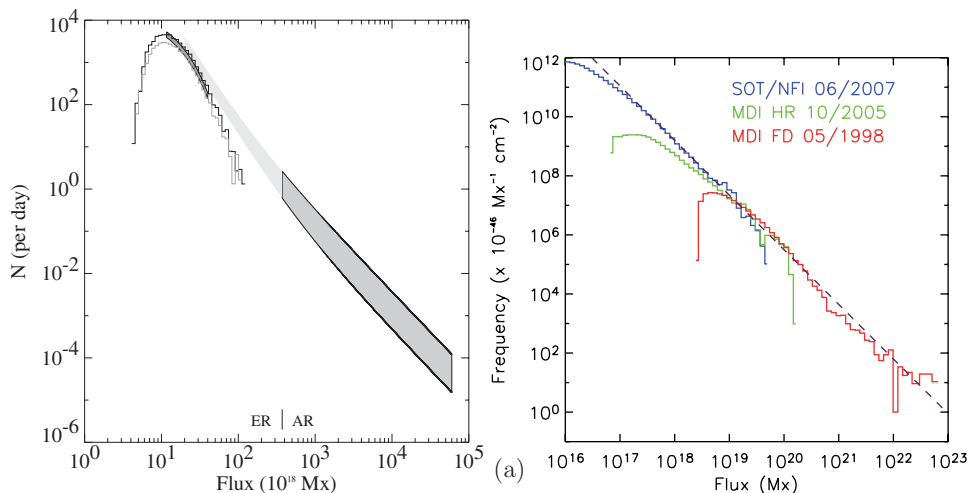
Fig. 8.19 *Left:* Composite distribution function of magnetic bipoles emerging on the Sun per day, per flux interval of 10^{18} Mx, and active regions (Hagenaar et al. 2003). *Right:* Synthesized histograms of magnetic features observed with SOT/Hinode and MDI/SOHO, identified with an automated clumping-feature algorithm. The combined powerlaw slope is $\alpha = 1.85 \pm 0.14$ (Parnell et al. 2009), (reproduced by permission of the AAS).

8.6.2 Solar Flares

There are only few studies that offer statistics on spatial scales of solar flares (Table 8.2). Area statistics of very small solar flares in the energy range of $E \approx 10^{24}$–3×10^{25} erg, called *EUV transient brightenings*, was sampled by Berghmans et al. (1998), finding an approximate powerlaw distribution with a slope of $\alpha_A = 2.7$ at a transition region wavelength (304 Å) and $\alpha_A = 2.0$ in a coronal wavelength (195 Å), measured with SOHO/EIT at spatial scales of $L \approx 3$–20 Mm. A similar SOHO/EIT study was conducted by Aletti et al. (2000), who measured the size of an EUV brightening from the number of pixels that have an intensity above a threshold of 2σ or 3σ, and obtained a (fractal area) size

Table 8.2 Frequency distributions of area sizes observed in solar flares. References: 1, Berghmans et al. (1998); 2, Aletti et al. (2000); 3, Aschwanden and Parnell (2002).

Events type	Wavelength of lengths	Range of areas L	Powerlaw slope α_A $N(A) \propto A^{-\alpha_A}$
EUV brightenings[1]	304 Å (He II)	3–20 Mm	2.7
EUV brightenings[1]	195 Å (Fe XII)	3–20 Mm	2.0
EUV brightenings (2σ)[2]	195 Å (Fe XII)	2–60 Mm	1.26 ± 0.04
EUV brightenings (3σ)[2]	195 Å (Fe XII)	2–20 Mm	1.36 ± 0.05
EUV nanoflares[3]	171, 195 Å	2–20 Mm	2.56 ± 0.23

distribution with powerlaw slopes of $\alpha_A = 1.26$–1.36 in the range of $A = 1$–$1,000$ pixels (corresponding to a length scale of $L \approx 2$–60 Mm). In a systematic study of EUV nanoflares detected with TRACE 171 and 195 Å, the (fractal) flare areas were measured with an elliptical area with length l and width w, yielding an area of $A = lw$ (Eq. 8.2.6). From a set of 281 automatically detected nanoflare events, size distributions of $N(l) \propto l^{-\alpha_l}$ with $\alpha_l = 2.10 \pm 0.11$ and $N(w) \propto w^{-\alpha_w}$ with $\alpha_w = 4.43 \pm 0.22$ and $N(A) \propto A^{-\alpha_A}$ with $\alpha_A = 2.56 \pm 0.23$ were found (Aschwanden and Parnell 2002), for a size range of $L \approx 2$–20 Mm.

Thus, there is very scarce statistics on distribution of spatial scales. A full-scale SOC model should also include geometric scaling laws, but little effort has been put into this aspect. What are our theoretical expectations for a geometric SOC model? One potential model is *Euclidean fragmentation*, which we envision simply by breaking down a solid structure into smaller space fragments. For instance, if we break a square-like chocolate into 16 equal pieces, each little square has a quarter length of the original size, so we have $N(L = 1) = 1$ and $N(L = 1/4) = 16$, and thus $N(L) \propto L^{-2}$. For solid structures, the expected scaling would then just be the reciprocal relationship of Euclidean scaling, e.g., $N(L) \propto L^{-1}$ for breaking a linear structure into smaller pieces, $N(L) \propto L^{-2} = A^{-1}$ for subdividing an area-like 2-D structure, and $N(V) \propto L^{-3} = V^{-1}$ for fragmenting a volume structure. For fractal geometries, we might expect a reciprocal scaling of the fractal dimension, but the definition of a length scale for fractal structures is more tricky. A comparison with the distributions measured in Table 8.2 shows at least some values are close to the expected scaling of $N(A) \propto A^{-1}$, but clearly more statistics is needed to narrow down more reliable values of the powerlaw slope based on a wider range of spatial scales.

There are some other area-related flare studies. The study of Sammis et al. (2000) investigated the flare peak fluxes as a function of the area of active regions and a trend was found that large active regions produce larger flares, but this general trend was found to be less significant than the dependence on the magnetic classification ($\alpha, \beta, \gamma, \delta$ classes of magnetic complexity of sunspots). In addition some studies explored whether the frequency distribution of peak fluxes in flares depends on the sizes of active regions and some systematic differences were found (e.g., Kucera et al. 1997; Sammis 1999) as expected for biased subsets, while the scale invariance was corroborated when compared among different active regions (Wheatland 2000c), which is expected for SOC models.

8.6.3 Lunar Craters

Craters can generally be produced either by volcanic eruptions or by meteoroid impacts, both representing violent catastrophic events that may exhibit SOC behavior. Many craters seen on the Moon or Earth appear to be the result of meteoroid impacts. Both the Moon and the Earth were subjected to intense bombardment between 4.6 and 4.0 billion years ago, which was the final stage of the sweep-up of debris left over from the formation of the solar system. The impact rate during that time was a thousand times higher than today's rate. Lunar craters, therefore, represent remnants or witnesses of catastrophic events that left a measurable imprint from which we can measure the size and perhaps even calculate the energy.
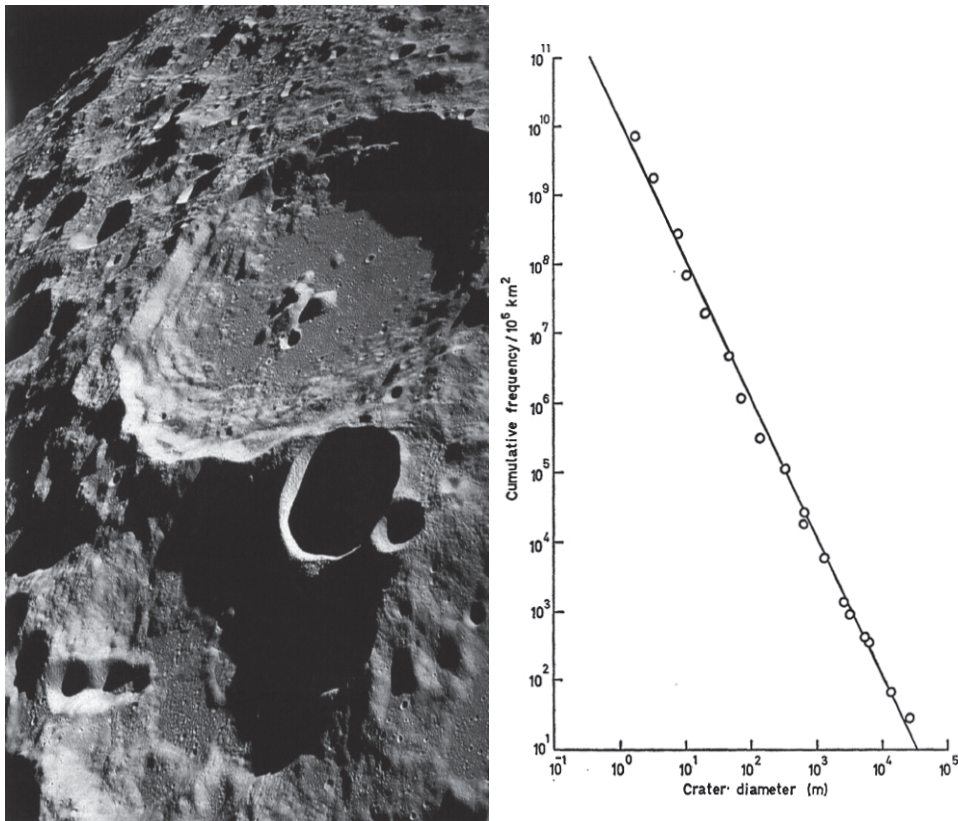
Fig. 8.20 *Left:* The lunar crater Daedalus, about 93 km in diameter, was photographed by the crew of Apollo 11 as they orbited the Moon in 1969 (NASA photo AS11-44-6611). *Right* Cumulative frequency distribution of crater diameters measured from *Ranger 8* in the lunar *Mare Tranquillitatis* (Cross 1966).

The size distribution of lunar craters was measured from pictures of the lunar orbiters *Ranger 7, 8, 9* by Cross (1966), who measured the diameters *L* from a total of 1,600 craters, ranging from 0.65 to 69,000 m, and found an approximate powerlaw function for the cumulative frequency distribution,

$$N^{cum}(>L) \propto L^{-2} \tag{8.6.1}$$

which corresponds to a differential frequency distribution of $N(L) \propto L^{-3}$ according to (Eq. 7.1.8). Cross (1966) conducted statistics of lunar craters for each Mare separately. One example of a cumulative frequency distribution of craters from the *Mare Tranquillitatis* using *Ranger 8* measurements is shown in Fig. 8.20 (right). A similar powerlaw index of 2.75 was also found for the size distribution of meteorites and space debris from man-made rockets and satellites (Fig. 3.11 in Sornette 2004).

Interpreting this result, we may think again of the concept of *Euclidean fragmentation*, for which we expect $N(L) \propto L^{-3}$. The more or less solid mass that was forming the solar system probably has been fragmented by collisions and tidal forces into smaller pieces. Conservation of mass and volume yields then the scaling law, $N(L) \propto L^{-3}$, since

$$V = N(L_0)L_0^3 = N(L)L^3 = \text{const} , \qquad (8.6.2)$$

where L_0 is the original average size and L is the smaller average size of fragments at a later time of the fragmentation process. The fragmentation process leads naturally to a self-similar fractal geometry, since fragments from frequent collisions tend to grind spherical objects, and combined with the spherically propagating shock waves during an impact event, leads also to a self-similar distribution of circular craters. Do impact craters qualify for a SOC system? Both the Euclidean fragmentation process (driven by two-body collisions) as well as the impact of a fragment on the lunar surface are both highly nonlinear dissipation processes, occur with a random waiting-time distribution, and exhibit scale-free powerlaw distributions of energies and sizes, and thus possess all typical characteristics of a SOC process. However, we cannot measure the time history of the event to obtain the peak energy, total energy, and duration, but are left with the imprints of the spatial sizes only.

8.6.4 Asteroid Belt

The asteroid belt between the planets Mars and Jupiter contains a large number of irregular bodies or minor planets with sizes from about 1,000 km (Ceres 1,020 km; Pallas 538 km; Vesta 549 km; Juno 248 km) down to the size of dust particles. While most planetesimals from the primordial solar nebula formed bigger planets under the influence of self-gravitation, the gravitational perturbations from the giant planets Jupiter and Saturn prevented a stable conglomeration of planetesimals in the zone between Mars and Jupiter, and thus we still live with a fragmented soup of primordial planetesimals, called the asteroid belt (Fig. 8.21, left). The asteroid belt has evolved into the present configuration by dynamical depletion due to the gravitational disturbance from the giant planets (which pull planetesimals into highly eccentric orbits) and collisions (which fragment the planetesimals further).

The asteroid size distribution has been studied in the *Palomar Leiden Survey* (Van Houten et al. 1970) and *Spacewatch Surveys* (Jedicke and Metcalfe 1998), where a power law of $N^{cum}(>L) \propto L^{-1.8}$ was found for the cumulative size distribution of larger asteroids ($L > 5$ km), which corresponds to a differential powerlaw slope of $\alpha_L \approx 2.8$. In a *Sloan Digital Sky Survey* collaboration (Fig. 8.21, right), a broken powerlaw was found with $N(L) \propto L^{-2.3}$ for large asteroids (5–50 km) and $N(L) \propto L^{-4}$ for smaller asteroids (0.5–5 km) (Ivezic et al. 2001). In the *Subaru Main-Belt Asteroid Survey*, a cumulative size distribution $N^{cum}(>L) \propto L^{-1.29 \pm 0.02}$ was found for small asteroids with $L \approx 0.6$–1.0 km (Yoshida et al. 2003; Yoshida and Nakamura 2007), which corresponds to a differential powerlaw slope of $\alpha_L \approx 2.3$.

Interpreting these results, which specify powerlaw slopes of the differential size distribution in the range of $\alpha_L \approx 2.3$–4.0, the average is close to the value $\alpha_L \approx 3$ expected
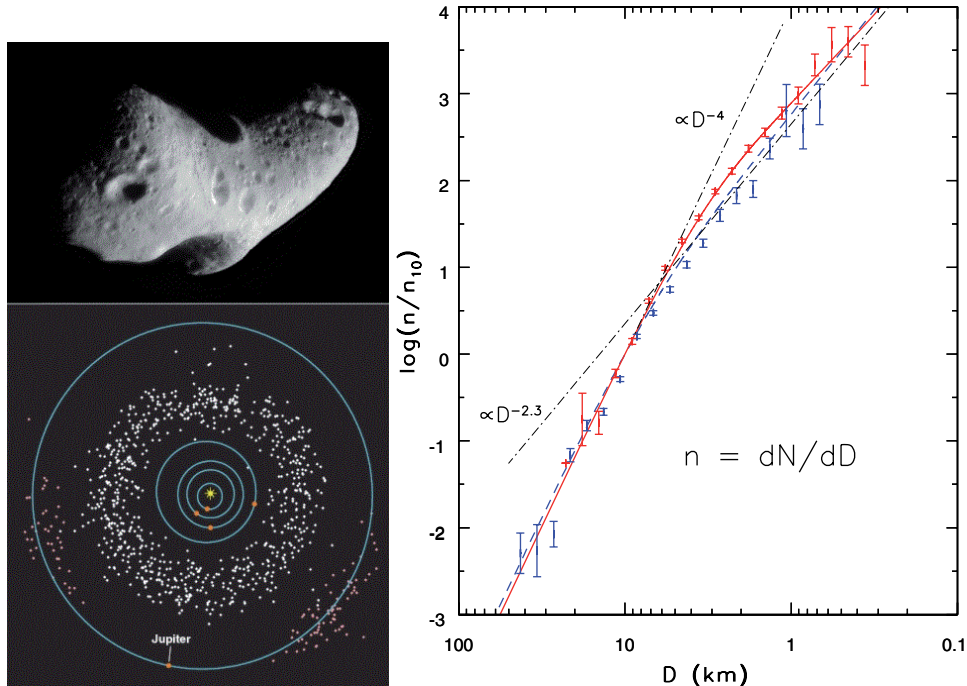
Fig. 8.21 *Left top:* A picture of the near-Earth asteroid *Eros* with a size of 30 km, pictured by a space probe. *Left bottom:* The main asteroid belt located between the Jupiter and Mars orbit. The subgroup of *Trojan asteroids* are leading and trailing along the Jupiter orbit. (Courtesy of NASA/Johns Hopkins University Applied Physics Laboratory). *Right:* Differential size distribution of asteroids observed in the *Sloan Digital Sky Survey* collaboration (Ivezic et al. 2001). (Reprinted with permission of Elsevier)

for Euclidean fragmentation, which predicts $N(L) \approx L^{-3}$, similar to the statistics of lunar craters (Section 8.6.3). However, the observational manifestation is quite different for these two phenomena, one observed before impact and the other after impact on a specific target. The fact that the size distribution exhibits a broken powerlaw could indicate that two different physical processes dominate in the two regimes, for instance dominant collisions with less gravitational orbit perturbation for the large asteroids ($L \gtrsim 5$ km), but stronger orbit perturbation and pre-dominant dynamic depletion for smaller asteroids. Nevertheless, a similar argument for asteroid formation as a SOC process can be made as for the creation of lunar craters.

8.6.5 Saturn Ring

Jupiter and Saturn are the two largest planets in our solar system, and thus it is no surprise that they also have numerous moons, rings, and ringlets thanks to their strong gravitational field. While the rings are located close to the planet (7,000 km to 80,000 km above Saturn's equator), the orbits of the moons are outside the rings. Mechanical resonances (i.e., in
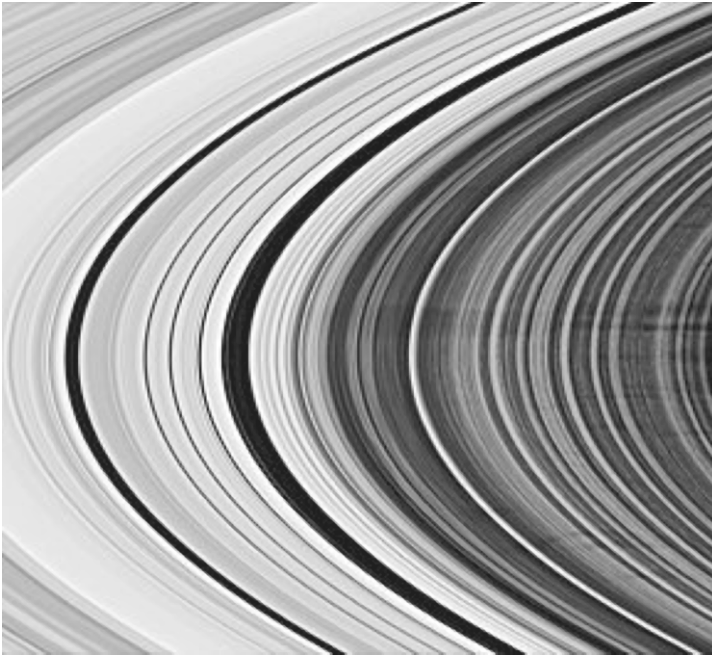
Fig. 8.22 Photo of Saturn's B-ring with Huygens gap, Cassini division, and spoke structures, recorded by the *Cassini* spacecraft (credit: NASA, JPL, Space Science Institute).

orbits that have a period with a harmonic ratio to the outer moons' periods) destabilize inner rings, leading to gaps (e.g., Encke gap, Cassini division), or stabilize the zones in between (Figs. 1.11 and 8.22). The Saturn ring consists of particles ranging from 1 cm to 10 m, with a total mass of 3×10^{19} kg, just about a little less than the moon Mimas. The origin of the ring was hypothesized to come either from nebular material left over from the formation of Saturn itself or from the tidal disruption of a former moon.

The distribution of particle sizes in Saturn's ring was determined with radio occultation observations using data from the *Voyager 1* spacecraft and a scattering model, which exhibited a powerlaw distribution of $N(r) \propto r^{-3}$ in the range of 1 mm $< r <$ 20 m (Zebker et al. 1985; French and Nicholson 2000). This result, again, is consistent with Euclidean fragmentation, similar to the distribution of sizes of asteroids (Section 8.6.4) and lunar craters (Section 8.6.3). Can we consider the evolution of the Saturn ring as a SOC process? Events are caused by collisional encounters, which probably occur at random time intervals (though very rare on human time scales) and the energy release during a collisional impact is likely to be a nonlinear dissipative (fragmentation) process, leading to powerlaw distributions of energies with some scaling to the powerlaw size distribution of the projectile and target. The critical threshold is some minimal velocity difference Δv (between the projectile and target body) for inelastic impacts with subsequent fracturing, while small Δv merely cause elastic reflections without catastrophic disintegration. Hence the same argument for a SOC process can be made as for asteroids and lunar craters.

8.7 Summary

SOC processes produce scale-free powerlaw-like size distributions of their dynamical parameters (peak energy, total energy, duration), which also extends to their geometric parameters (length, area, volume). The powerlaw-like size distributions of geometric parameters then consequently imply also powerlaw-like scaling laws between geometric parameters, such as $A(L) \propto L^{D_A}$ and $V(L) \propto L^{D_V}$. These geometric scaling laws can be either Euclidean ($D_A = 2$ and $D_V = 3$) or fractal ($D_A < 2$ and $D_V < 3$). Cellular automaton models of SOC processes can reproduce fractal geometries in the spatial propagation of avalanches, and thus fractal scaling laws are expected for most SOC processes. We discussed 1-D fractals (Section 8.1), which can be applied to 1-D time series of astrophysical observations (e.g., variability of solar radio emission). Measuring 2-D fractals (Section 8.2) can be done most conveniently in astrophysical images inside our solar system (e.g., magnetospheric substorms, solar photosphere, or solar flares). The derivation of 3-D fractal dimensions (Section 8.3) is more tricky, because it requires either geometric models or lattice-based computer simulations. The measurement of fractal characteristics can be done either by box-counting algorithms (Section 8.2), multifractal analysis (Section 8.4), spatial power spectrum analysis (Section 8.5), or by statistics of spatial scales (Section 8.5). With the latter method we explored magnetic structures in the solar photosphere as well as during flares and found them all to be fractal. In contrast, the size distribution of lunar craters, asteroids, and Saturn ring particles all exhibit a Euclidean scaling law of $N(L) \propto L^{-3}$, as expected for a fragmentation process. In summary, fractal or Euclidean scaling laws of geometric parameters and their powerlaw-like size distributions are necessary conditions for SOC processes, but not sufficient to prove a SOC process, because non-SOC processes (such as intermittent turbulence) can also produce powerlaw-like distributions of spatial scales.

8.8 Problems

Problem 8.1: What is the 1-D ("Sierpinski dust") and 3-D analog ("Sierpinski tetrahedron") of the 2-D Sierpinski triangle shown in Fig. 8.6. Calculate their fractal dimensions.

Problem 8.2: Construct a time series (say $N = 10,000$ points) with a random generator and measure its fractal dimension with the method of Higuchi (Section 8.1.2). Smooth the time series with a box-car of $n_{sm} = 10$ and 100 and determine its fractal dimension. How much smoothing is needed to obtain a near-Euclidean dimension of $D \approx 1$ within 1%?

Problem 8.3: Download digital astronomical images of a spiral galaxy, a globular cluster, and a star field. Measure their fractal dimensions for various thresholds (say 10%, 20% and 50% of the maximum intensity). In which cases do you obtain a near-Euclidean dimension of $D = 1$ as expected for dot-like stars. Which case shows the highest fractal dimension and what spatial structure is it associated with?

Problem 8.4: Verify the analytical expressions of the area- q_A and volume-filling factors q_V given Eqs. 8.3.8–8.3.10 for an aspect angle of $\alpha = 0°$ by means of a Monte-Carlo

simulation for $n_{loop} = 10, 100$, and 1,000 loop elements in a half-cylinder configuration as shown in Fig. 8.15.

Problem 8.5: Design a simple Monte-Carlo simulation for the fragmentation of planetesimals, assuming that collisions occur in random time intervals and between random fragments, where each collision splits a planetesimal into two half volumes. Sample the size distribution $N(L)$ after 10^3, 10^4 and 10^5 events and fit a powerlaw distribution $N(L) \propto L^{-\alpha_L}$. Do you find a Euclidean dimension of $\alpha_L = 3$? Think of improvements that would make the model more realistic.